



Article

Bioinspired Synthesis of Magnetic Nanoparticles Based on Iron Oxides Using Orange Waste and Their Application as Photo-Activated Antibacterial Agents

David Giancarlo García ¹, Cristina Garzón-Romero ², Mateo Alejandro Salazar ², Karina J. Lagos ¹, Kleber Orlando Campaña ¹, Alexis Debut ³, Karla Vizuete ³, Miryan Rosita Rivera ², Dario Niebieskikwiat ⁴, Maria J. Benitez ⁵ and María Paulina Romero ^{1,*}

- ¹ Department of Materials, Escuela Politécnica Nacional (EPN), Quito 170525, Ecuador
² Laboratorio de Investigación en Citogenética y Biomoléculas de Anfibios (LICBA), Centro de Investigación para la Salud en América Latina (CISeAL), Facultad de Ciencias Exactas y Naturales, Pontificia Universidad Católica del Ecuador (PUCE), Quito 170143, Ecuador
³ Centro de Nanociencia y Nanotecnología, Universidad de Las Fuerzas Armadas ESPE, Sangolquí 171103, Ecuador
⁴ Departamento de Física, Colegio de Ciencias e Ingenierías, Universidad San Francisco de Quito, Quito 170901, Ecuador
⁵ Departamento de Física, Escuela Politécnica Nacional (EPN), Quito 170525, Ecuador
* Correspondence: maria.romerom@epn.edu.ec

Abstract: Magnetic nanoparticles based on iron oxides (MNPs-Fe) have been proposed as photothermal agents (PTAs) within antibacterial photothermal therapy (PTT), aiming to counteract the vast health problem of multidrug-resistant bacterial infections. We present a quick and easy green synthesis (GS) to prepare MNPs-Fe harnessing waste. Orange peel extract (organic compounds) was used as a reducing, capping, and stabilizing agent in the GS, which employed microwave (MW) irradiation to reduce the synthesis time. The produced weight, physical–chemical features and magnetic features of the MNPs-Fe were studied. Moreover, their cytotoxicity was assessed in animal cell line ATCC RAW 264.7, as well as their antibacterial activity against *Staphylococcus aureus* and *Escherichia coli*. We found that the 50GS-MNPs-Fe sample (prepared by GS, with 50% v/v of NH₄OH and 50% v/v of orange peel extract) had an excellent mass yield. Its particle size was ~50 nm with the presence of an organic coating (terpenes or aldehydes). We believe that this coating improved the cell viability in extended periods (8 days) of cell culture with concentrations lower than 250 µg·mL⁻¹, with respect to the MNPs-Fe obtained by CO and single MW, but it did not influence the antibacterial effect. The bacteria inhibition was attributed to the plasmonic of 50GS-MNPs-Fe (photothermal effect) by irradiation with red light (630 nm, 65.5 mW·cm⁻², 30 min). We highlight the superparamagnetism of the 50GS-MNPs-Fe over 60 K in a broader temperature range than the MNPs-Fe obtained by CO (160.09 K) and MW (211.1 K). Therefore, 50GS-MNPs-Fe could be excellent candidates as broad-spectrum PTAs in antibacterial PTT. Furthermore, they might be employed in magnetic hyperthermia, magnetic resonance imaging, oncological treatments, and so on.

Keywords: green synthesis; antibacterial PTT; iron oxide nanoparticles; orange peel extract; cytotoxicity; superparamagnetic behavior



Citation: García, D.G.; Garzón-Romero, C.; Salazar, M.A.; Lagos, K.J.; Campaña, K.O.; Debut, A.; Vizuete, K.; Rivera, M.R.; Niebieskikwiat, D.; Benitez, M.J.; et al. Bioinspired Synthesis of Magnetic Nanoparticles Based on Iron Oxides Using Orange Waste and Their Application as Photo-Activated Antibacterial Agents. *Int. J. Mol. Sci.* **2023**, *24*, 4770. <https://doi.org/10.3390/ijms24054770>

Academic Editor: Sandra Pinto

Received: 21 December 2022

Revised: 26 January 2023

Accepted: 31 January 2023

Published: 1 March 2023



Copyright: © 2023 by the authors. Licensee MDPI, Basel, Switzerland. This article is an open access article distributed under the terms and conditions of the Creative Commons Attribution (CC BY) license (<https://creativecommons.org/licenses/by/4.0/>).

1. Introduction

Bacterial infections are a potential cause for developing chronic diseases in patients, producing severe health problems and leading to death [1]. The uncontrolled use of antibiotics has contributed to the development of multidrug-resistant (MR) bacteria [2–4]. Since bacteria can proliferate on most surfaces (prosthetics catheters, medical equipment, hospital ventilation ducts, open wounds, food, etc.) [5,6], they have become a potential risk. Thus, bacteria MR infections are considered one of the three primary health problems of

the 21st century, which will cause 300 million deaths with an economic loss greater than USD 100 trillion in the next 28 years [7].

Nanotechnology has contributed to finding solutions to this problem, developing antibacterial nanomaterials, e.g., carbon-based nanomaterials such as graphene oxide, reduced graphene oxide, carbon dots, and carbon nanotubes [5,8]. Additionally, metal nanoparticles (NPs) such as AgNPs, AuNPs, PtNPs, etc. [9], and metal-oxide-based nanomaterials including magnetite (Fe_3O_4) NPs, maghemite ($\gamma\text{-Fe}_2\text{O}_3$) NPs [10], nanocomposites (NCs) of Ag-TiO₂ or hydroxyapatite (HAp) doped with magnetic ions (Sr/Fe) have been employed to combat this issue due to their intrinsic antibacterial activity, and, according to their nature, they can inhibit Gram-positive and Gram-negative bacteria by different mechanisms [1,11–13]. For example, Fe_3O_4 -NPs, NCs of Ag-TiO₂, have shown antibacterial activity against *Staphylococcus aureus* (*S. aureus*) and *Escherichia coli* (*E. coli*) depending on their concentration and high reactive oxygen species (ROS) generation capacity [14,15]. Likewise, NCs of HAp and Fe_3O_4 work against *Micrococcus luteus* and *E. coli* [16]. In several cases, the antimicrobial activity of the cited nanomaterials can be enhanced with functionalizing agents (antibiotics, polymers, organic molecules, etc.) [17–19] or by incorporating therapies such as photodynamic therapy (PDT) and PTT [20–22].

To obtain these nanomaterials, green synthesis (GS) has been proposed, which presents notable advantages because when using plant extracts from leaves, fruits, seaweeds, and so on [23], organic molecules are available that take the role of reducing, capping, and stabilizing agents [24,25] at once, and depending on the green extract, it can provide molecules with antibacterial properties. For example, Potbhare et al. [26] synthesized CuO nanospheres using *Phyllanthus reticulatus*, where their nanospheres enhanced bacterial inhibition in *E. coli*, *Klebsiella pneumoniae*, and *S. aureus* strains. In addition, the GS of MNPs-Fe proposes reducing or replacing the conventional agents that are dangerous in their handling and have toxic composition, e.g., ammonium hydroxide (NH_4OH) or sodium hydroxide (NaOH) [27–31], typically used in MNPs-Fe synthesis, such as coprecipitation [32], sol-gel [33], hydrothermal [34], or solvothermal methods [35], among others [36–38]. Hence, the GS becomes easy and environmentally friendly [39].

The use of plant extracts in the GS of MNPs-Fe incorporates the circular economy concept due to the use of organic waste from the food industry [40]. Likewise, GS allows incorporating heating by microwave (MW) irradiation, achieving higher reaction rates and thus reducing synthesis times due to rapid and homogeneous volumetric heating (rotation of electric dipoles and ions) compared to conventional heating methods, e.g., heating by flame or electric resistance [41–44].

On the other hand, antibacterial PTT uses light irradiation, typically in the near-infrared (NIR, 700–1350 nm, optical window) [45], to raise the temperature to $\sim 50^\circ\text{C}$ of PTAs [46,47], which host bacteria cell membranes or internalize by several mechanisms such as passive diffusion or receptor-mediated endocytosis, among others [1,48,49], causing irreversible damage in the cell membrane and protein disruption, which leads to bacterial death [20]. When using MNPs-Fe as PTAs, a characteristic effect is achieved, known as localized surface plasmonic resonance (LSPR). The electric field of NIR light induces collective resonant oscillation of free electrons (electron cloud) of the MNPs-Fe, due to the absorbed photons, which are converted into phonons, increasing the temperature in the crystal lattice of the MNPs-Fe [47]. For this reason, MNPs-Fe are excellent candidates as broad-spectrum antibacterial agents in antibacterial PTT [4,50].

Regarding cytotoxicity, the toxic effect of MNPs-Fe at a cellular level has been studied in healthy eukaryotic cells (e.g., fibroblasts, liver cells, stem cells derived from adipose tissue, etc.) [51,52] and diseased cells (mainly cancer cells, e.g., DU-145, LNcaP, HeLa, MCF-7, etc.) [10,53,54], as well as in prokaryotic cells, e.g., *S. aureus*, *E. coli*, and so on (a toxic effect on bacteria known as antibacterial activity) [13,18,55]. In any case, the cytotoxic effect depends on the concentration of the MNPs-Fe. Similar mechanisms of cell damage are present in prokaryotic and eukaryotic cells. The MNPs-Fe induce oxidative stress by generating reactive oxygen species (ROS). It releases Fe ions (Fe^{+2} , Fe^{+3}) that

create an acidic environment and, in the presence of H_2O_2 , produce $\bullet OH$ radicals (Fenton reaction) that depolymerize polysaccharides and inactivate enzymes, lipid peroxidation, and DNA damage. MNPs-Fe can also cause mechanical disruption by localizing to the cell membrane [18,56]. However, in the human body, endocytosis is a crucial mechanism by which cells interact with large or small particles. The phagocytes use their plasma membrane to engulf NPs (phagocytosis) or, in turn, are inhibited by forming a crown of non-specific proteins, producing unpredictable pharmacokinetics [57]. Thus, their size, morphology, and surface chemistry play an essential role in the interaction with target cells; e.g., the kidneys remove NPs of a size < 10 nm and the liver removes NPs of a size > 10 nm, which can also be phagocytized [33,34].

Biotherapies, such as oncology, seek to improve biodistribution times to reach the target cells. Thus, to improve the availability of NPs in the biological environment, they typically are functionalized with polymeric molecules such as polyethylene glycol (PEG), which produces a protein repulsion effect, or molecules of interest that allow increasing selectivity toward target cells [58]. In this sense, GS is also beneficial due to the great availability of organic molecules. In the case of MNPs-Fe, their superparamagnetism (SPM) behavior makes the magnetic targeting towards the required zone possible. Certainly, the surface chemistry and size of the NPs govern their interaction with the target cell [18]. In the case of MNPs-Fe with SPM behavior, it makes the targeting toward the required zone possible. To achieve SPM behavior, uniform size distribution (< 100 nm) of the MNPs-Fe and a non-interacting system are essential, i.e., an adequate concentration of MNPs-Fe that does not allow the formation of agglomerates and the MNPs-Fe do not interact with each other in close proximity [59]. Avoiding the agglomeration of NPs is an intrinsic challenge in the synthesis routes of nanomaterials and makes it difficult to adequately develop bio-applications [60].

The current study proposes a fast and simple GS to obtain MNPs-Fe. MW irradiation, iron precursors, ammonium hydroxide, and orange peel extract were employed to achieve this aim. Regarding the organic extract, it came from waste produced by street orange juice vendors. The organic compounds within the orange peel extract constitute reducing agents in combination with low amounts of ammonium hydroxide. To compare the properties of the as-prepared MNPs-Fe, we also carried out different syntheses using the coprecipitation (CO) method and irradiating with MW without the organic extract. We evaluated the produced weight of GS, the antibacterial activity within PTT, cytotoxicity, SPM behavior of the MNPs-Fe, and the effects of the incorporation of organic molecules into de MNPs-Fe compared to others obtained by CO and MW.

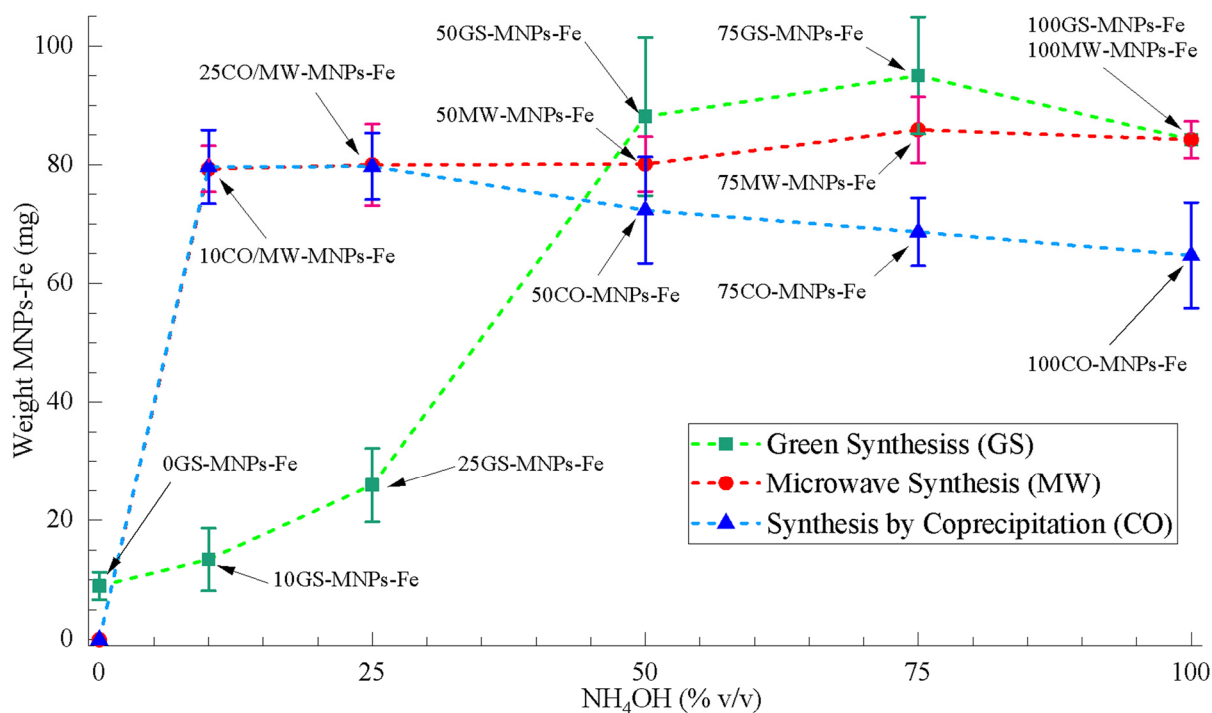
2. Results and Discussion

2.1. Weight Obtained of MNPs-Fe

Quantification of the yield in mass is essential to evaluate the potential scaling of the synthesis at an industrial level. To obtain the mass yield of the GS, CO, and MW syntheses (from the weight of the precursors and the MNPs-Fe obtained, see Table 1), the MNPs-Fe samples were dried (see Section 2.3), and triplicate tests were carried out. Figure 1 presents the average weights obtained for each synthesis. This information is detailed in Table S1. These results indicated that GS produced a higher weight of MNPs-Fe for NH_4OH (% v/v) between ~ 50 and 100% v/v. The 100GS-MNPs-Fe and 100MW-MNPs-Fe samples are the same, i.e., they had 100% v/v of NH_4OH and were synthesized under the same conditions without orange peel extract. In the concentration range of NH_4OH (% v/v) 0 to ~ 50 % v/v, the GS produced weight is considerably reduced compared to CO and MW, which maintain their produced weight. However, the role of the organic molecules of the orange peel extract as a reducing agent stands out because, in the absence of NH_4OH , 0GS-MNPs-Fe were achieved in small quantities (8.97 ± 2.32 mg). In turn, at 0% v/v of NH_4OH in CO, MW did not crystallize MNPs-Fe. Only DI water was added to the precursor solution, reducing its concentration without generating any reaction.

Table 1. Mass yield and iron oxide phases of MNPs-Fe obtained by GS, MW, and CO syntheses.

Sample	Mass Yield	Phases
0GS-MNPs-Fe	1.12%	35.3% Magnetite, 64.7% Hematite
25GS-MNPs-Fe	3.71%	39.5% Magnetite, 53% Maghemite, 7.5% Hematite
50GS-MNPs-Fe	29.36%	47.0% Magnetite, 53.0% Maghemite
75GS-MNPs-Fe	18.40%	47.0% Magnetite, 53.0% Maghemite
100GS-MNPs-Fe	91.50%	6.6% Magnetite, 93.4% Maghemite
25CO-MNPs-Fe	89.08%	88.0% Magnetite, 12.0% Maghemite
50CO-MNPs-Fe	80.15%	63.5% Magnetite, 36.5% Maghemite
75CO-MNPs-Fe	74.69%	8.9% Magnetite, 91.1% Maghemite
100CO-MNPs-Fe	72.56%	98.0% Magnetite, 2.0% Maghemite
25MW-MNPs-Fe	87.73%	34.1% Magnetite, 65.9% Maghemite
50MW-MNPs-Fe	89.59%	91.2% Magnetite, 8.8% Maghemite
75MW-MNPs-Fe	93.43%	10.0% Magnetite, 90.0% Maghemite

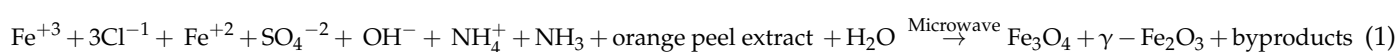
**Figure 1.** Weight curves of MNPs-Fe obtained from GS, CO, and MW with respect to the NH_4OH (% v/v).

It is essential to indicate that the magnetic character of the sample 0GS-MNPs-Fe was not stable, i.e., this solution lost its magnetism in short periods (24–48 h). The low stability of 0GS-MNPs-Fe can be justified due to the oxidation of the magnetite and maghemite on the surface of a large number of organic molecules available (100% v/v of orange peel extract), as suggested by Lopez G. et al. [61].

In GS, it is complex to establish a formation reaction of the MNPs-Fe, owing to the great variety of organic compounds. We must consider that the orange peel extract differs according to the place and period of the orange harvest [31,62]. It is known that Fe^{+2} and Fe^{+3} ions form intermediate compounds such as $\text{Fe}(\text{OH})_2$ and $\text{Fe}(\text{OH})_3$ to generate Fe_3O_4 and water [63]. Hence, the availability of OH^- ions in the reducing agent's solutions is crucial in synthesizing MNPs-Fe. For this reason, the pH (function of the H^+ concentration) in the reducing agent's solutions and the byproducts of the synthesis (GS, CO, and MW) were studied (see Figure S1). The acid character of the orange peel extract (pH = 5.15) did not significantly influence the pH of the reducing agent's solutions in GS, and it remained

between 11.59 and 13.16 for solutions between 10 and 100% v/v of NH_4OH , i.e., a similar availability of hydroxyl ions (OH^-) in any case (CO and MW). Likewise, GS and MW product pH measurements were more environmentally friendly (pH = 7.20–8.76) than CO (pH = 9.74–11.11). The pH measurements were consistent with the produced weight of GS and MW since the synthesis consumed a more significant amount of OH^- ions to form MNPs-Fe. However, in GS, for 0 to ~50% v/v of NH_4OH , a significant amount of available organic molecules can interact with the OH^- reducing the obtained weight of MNPs-Fe. In the specific case of 0GS-MNPs-Fe, the byproducts were acidic (pH = 1.52) because the few available OH^- were consumed, increasing the concentration of H^+ .

Equation (1) proposes a possible mechanism for the formation of MNPs-Fe by GS according to the precursors and reducing agents used in this work, where the quantity and type of molecules from the orange peel extract is a factor that influences the weight obtained of MNPs-Fe. Equation (1) was adjusted from the proposal made by Palash D. et al. [39], who used *Lathyrus sativus* peel extract.



The sample 50GS-MNPs-Fe was selected to develop the cytotoxicity and antibacterial PTT studies for their high weight obtained (88.13 ± 13.33 mg) and low NH_4OH consumption (greater green approach) compared to samples 75GS-MNPs-Fe (95.03 ± 9.85 mg) and 100GS-MNPs-Fe (84.20 ± 3.10 mg). In addition, its weight obtained was comparable to that of 50MW-MNPs-Fe (80.10 ± 4.61 mg) and 50CO-MNPs-Fe (72.33 ± 8.96 mg), which did not occur for the lower 50% v/v of NH_4OH samples in GS.

To have comparative results, the mass yield of Fe was calculated from the amount of Fe in the precursors and the Fe present in the obtained MNPs-Fe, and these are shown in Table 1. The results acquired in XRD and EDS were considered.

The mass yields of the synthesis by CO and MW were similar to those reported in analogous studies (62–97%) [64–66] that use Fe salt-type precursors. GS generated low yields by mass (1.12–29.36%), except for the 100GS-MNPs-Fe sample (without extract). This stands out with the results reported by E. Nnadozie et al. (3–85%) [67]. However, in the synthesis that we propose in this study, the synthesis time is considerably reduced (a few minutes) compared to the 14 days reported by E. N et al., which includes drying *Chromolaena odorata* leaves, used as a green extract. This is due to using microwaves and vegetable extract in the liquid state. Likewise, reducing the amount of magnetic phase allows the incorporation of organic molecules, which provide additional benefits to the as-synthesized MNPs-Fe.

2.2. MNPs-Fe Characterization

2.2.1. Morphology, Size Distribution, and Topography of MNPs-Fe

The SEM images of the samples obtained by GS allowed us to identify a quasi-spherical morphology and a normal size distribution; see Figure S2. The 50GS-MNPs-Fe sample had an average size of 49.3 ± 9.6 nm, the smallest of the GS samples (see Figure 2a). A few agglomerates were also found and neglected to determine the average size of the MNPs-Fe. DLS analysis allowed the study of the hydrodynamic diameter of the 50GS-MNPs-Fe sample. Thus, two populations of different sizes were observed; see Figure 2b. In DLS, a model based on the intensity of the scattered electric field for polydisperse particles was used, which presents intensity contributions according to the hydrodynamic radius of the populations present. Therefore, the highest intensity does not refer to the population quantity of MNPs-Fe [68]. This result corroborates that the few agglomerates observed in SEM comprised the 224.8 ± 0.4 nm population. The 74.7 ± 0.1 nm population corresponds to the 50GS-MNPs-Fe size coated with organic molecules from the orange peel extract, which is consistent with the study developed by Bano S. et al. [31]. This shell of organic molecules has a thickness of 25.4 nm, as indicated in Figure 2b. It is necessary to highlight that the SEM images show the naked MNPs-Fe.

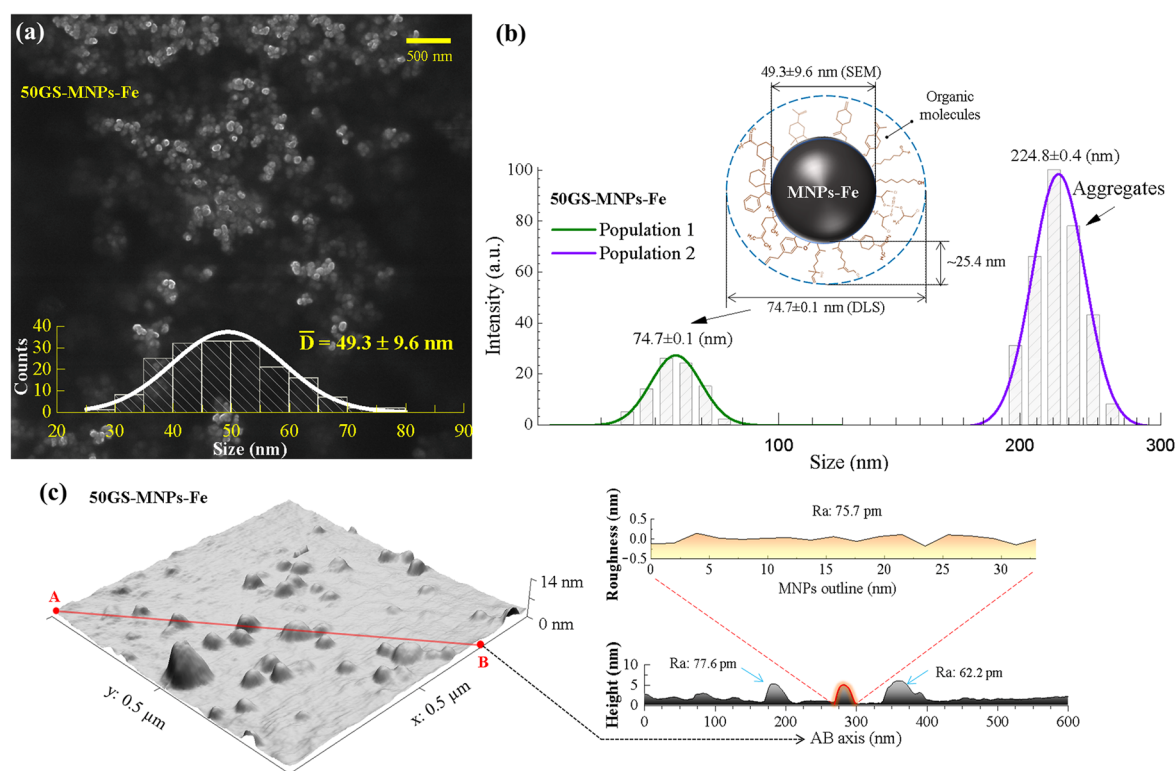


Figure 2. The 50GS-MNPs-Fe sample: (a) SEM image, (b) hydrodynamic size distribution obtained by DLS and (c) AFM image along with two-dimensional topography profiles.

The AFM topography of the GS samples enabled the study of the average roughness (Ra) of the MNPs-Fe and corroborated a quasi-spherical morphology. Figure 2c corresponds to the topography of the 50GS-MNPs-Fe sample. The contours of the MNPs-Fe (red curve) in two-dimensional profiles along an arbitrary axis (e.g., AB axis in Figure 2c) acquired from Gwyddion 2.60 software empowered us to study Ra. Consequently, 20 random measurements of Ra were achieved in different contours and profiles of the MNPs-Fe, omitting regions of agglomerates and without MNPs-Fe. To estimate a representative Ra of the scanned section, Ra was measured in 20 profiles of the MNPs-Fe. This was achieved by taking AB axes randomly, which comprise different MNPs-Fe, and avoiding agglomerates. The values of Ra increased according to the amount of orange peel extract used in GS; see Table S2. The 50GS-MNPs-Fe sample showed an $Ra = 78 \pm 22$ pm, while 100GS-MNPs-Fe (without orange peel extract) exhibited an $Ra = 58 \pm 12$ pm. Thus, in GS, the shell of MNPs-Fe formed by organic molecules from the orange peel extract increases the value of Ra. Furthermore, it is essential to consider that the Ra values are sensitive to pixel resolution and size [69]. Likewise, Ra can be affected by the interaction between the AFM tip (Tapping mode) and the organic molecules bound to the MNPs-Fe since this superficial organic crown is approximately 24.2 nm (DLS) and can be considered a soft sample, as suggested by Christensen M. et al. [70].

2.2.2. Phase and Chemical Composition of the MNPs-Fe

The diffraction patterns of the MNPs-Fe, obtained by GS, MW, and CO, presented phases of magnetite (Fe_3O_4) and maghemite (Fe_2O_3). Their relative peak positions (2θ) most coincided with crystallographic charts reported in the Crystallography Open Database (COD) to magnetite; see Figure S3a–c. Nevertheless, the characteristic peaks of the organic molecule shell in these samples could reduce the intensity of the characteristic peaks of magnetite [17]. The XRD patterns of the samples obtained by CO and GS presented relative

peak positions and intensities coinciding with the COD crystallographic charts because these MNPs-Fe do not have an organic shell; see Figure S4b,c.

Figure 3a shows the XRD patterns of 50GS-MNPs-Fe, 50MW-MNPs-Fe, and 50CO-MNPs-Fe samples. In the three cases, the characteristic peaks of magnetite and maghemite were observed at 2θ : 18.4° (111), 30.2° (220), 35.5° (311), 37° (222), 43.1° (400), 53.4° (242), 57.1° (511), 62.8° (440), 74.1° (533) and 89.5° (713) [71,72], matching with the crystal charts of COD. The 50GS-MNPs-Fe sample corresponded to magnetite COD ID 1011032 (cubic system, Fd-3m) and maghemite COD ID 9006316 (cubic system, Fd-3m) with a contribution of 47.0% and 53.0%, respectively. The 50MW-MNPs-Fe sample was identified as magnetite COD ID 9005842 (cubic system, Fd-3m) and maghemite COD ID 1528612 (cubic system, P4₁32), with a contribution of 91.2% and 8.8%, respectively. Likewise, the 50CO-MNPs-Fe sample coincided with magnetite COD ID 9002319 (cubic system, Fd-3m) and maghemite COD ID 9006317 (cubic system, P4₁32) in a contribution of 63.5% and 36.5%, respectively. This identification was carried out in the Match! 3 software. See Table 1 for all samples. The contribution of magnetite, maghemite, and hematite in the 0GS-MNPs-Fe, 25GS-MNPs-Fe, 50GS-MNPs-Fe, and 75GS-MNPs-Fe samples are not absolute since they have a contribution of organic molecules from the green synthesis.

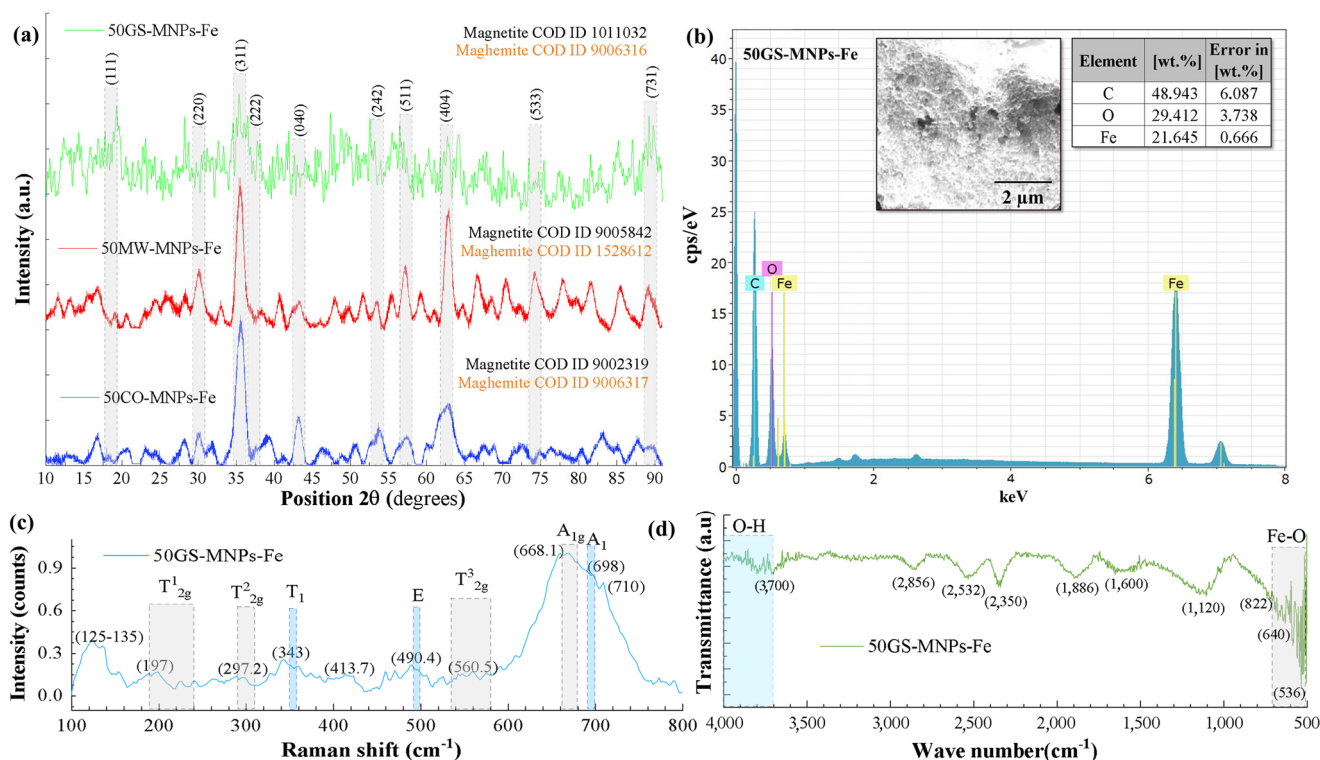


Figure 3. (a) XRD patterns of 50GS-MNPs-Fe, 50MW-MNPs-Fe, and 50CO-MNPs-Fe samples; 50GS-MNPs-Fe sample: (b) EDS spectrum and elemental composition (wt. %), (c) Raman spectrum between 100 and 800 cm^{-1} and (d) FT-IR spectrum.

The XRD pattern of 50GS-MNPs-Fe shows many additional peaks. These peaks might correspond to organic molecules of the orange peel extract (MNPs-Fe shell), which have a crystalline structure, for example, crystalline cellulosic components with characteristic peaks at 2θ : 15° , 22° and 35° [73]. Likewise, compounds such as Linalool and Eugenol reported in orange peel [31,62] have characteristic peaks at 2θ : 11.7° , 15.7° , 17.2° , 21.4° , 22.5° , 23.6° and 30.2° [74]. The crystallite size (D_c) was calculated using the Scherrer equation [75], and the FWHM (full width at half maximum) value was obtained using the OriginPro2018 software using a Voigt-type nonlinear fit on the peaks corresponding to the planes (131) (greater intensity). The Scherrer constant $k = 0.89$, typical for spherical geometries, was considered. The D_c of the 50GS-MNPs-Fe, 50MW-MNPs-Fe, and 50CO-MNPs-Fe samples

was 10.97 nm, 10.25 nm, and 7.84 nm, respectively. Table S4 presents D_c , lattice parameters, FWHM, and 2θ corresponding to all the samples described in Table 1. D_c refers to coherent diffracting crystalline domains as indicated by various studies [76–78]. Therefore, the smaller D_c size than the sizes obtained by SEM suggests that the MNPs-Fe are composed of several crystallites generated by stacking defects in the nucleation of the MNPs-Fe [76].

The EDS elemental analysis (Figure 3b) allowed identifying the presence of carbon (C), oxygen (O), and iron (Fe) in the 50GS-MNPs-Fe sample. The high weight percentages of C ($48.847 \pm 6.087\%$), O ($29.298 \pm 3.7\%$), and Fe ($21.487 \pm 0.666\%$) were consistent with the XRD results, i.e., magnetite, maghemite phases and a shell of carbon-based organic molecules. In the samples obtained by GS, the C content (wt. %) increased according to the amount of orange peel extract used in the synthesis; see Figure S4.

Raman spectra were acquired in the range of $100\text{--}2000\text{ cm}^{-1}$. Nonetheless, the active Raman bands for magnetite and maghemite are within $100\text{--}800\text{ cm}^{-1}$ [46,47]. Therefore, Figure 3c shows the Raman spectrum of the 50GS-MNPs-Fe sample in $100\text{--}800\text{ cm}^{-1}$. The gray regions correspond to characteristic Raman bands of magnetite, and the light blue ones to characteristic bands of maghemite [79–81]. Active bands of magnetite were observed at 197 cm^{-1} (T_{2g}^1 , translational movement of the Fe_3O_4 structure), 297.2 cm^{-1} (T_{2g}^2 , asymmetric stretching of Fe and O), 560.5 cm^{-1} (T_{2g}^3 , asymmetric bending of O with respect to Fe), and 668.1 cm^{-1} (A_{1g} , symmetric stretching of O along Fe-O bonds) consistent with reports of active bands of magnetite [36]. Likewise, the maghemite active bands observed were 343 cm^{-1} (T_1 , asymmetric stretching Fe-O), 490.4 cm^{-1} (E, symmetric bending O along Fe-O bonds), and 698 cm^{-1} (A_1 , symmetric stretching Fe-O) similar to the bands reported in [82,83]. The bands $125\text{--}135\text{ cm}^{-1}$ correspond to the vibration of crystalline structures (LA-Modes) [84]. The band observed at 413.7 cm^{-1} was attributed to the symmetrical stretching between O external to magnetite and maghemite with Fe ions belonging to iron oxides [84]. The Raman spectrum of the 50GS-MNPs-Fe sample was compared to magnetite (record ID 319 obtained from the HORIBA database), generating a 79.32% correlation with the help of Wiley Science's KnowItAll software.

The complete Raman spectrum (see Figure S5) allowed identifying active bands of molecule bonds that cover the 50GS-MNPs-Fe sample (derived from orange peel extract). Table S3a shows the Raman active bands observed, with their molecular vibrations according to atomic bonds and the possible molecules present.

Figure 3d shows the FT-IR spectrum of the 50GS-MNPs-Fe sample. Active bands were observed between $600\text{--}450\text{ cm}^{-1}$, corresponding to vibrations between Fe-O atoms of the magnetite and maghemite phases [85–88]. Organic molecules' active FT-IR bands were also observed and are shown in Table S3b. The FT-IR active band at 2532 cm^{-1} (S compounds) can be generated by ions (SO_4^{2-}) derived from Fe^{2+} sulfate. Likewise, the halogens are due to ions (Cl^-) from Fe^{3+} chloride used as a precursor. Additionally, the $2,350\text{ cm}^{-1}$ band of amine salts suggests the formation of compounds derived from NH_4OH .

Table S3a,b were developed according to the active bands reported by Horiba J. [84] for the analysis of Raman and FT-IR spectra, as well as the studies carried out by S. Bano et al. [31] and G. Kahrilas et al. [62].

Using FT-IR and Raman spectroscopy, the presence of magnetite and maghemite was corroborated, as well as the functionalization of the 50GS-MNPs-Fe with organic molecules of the type alcohols, aldehydes, S compounds, amines, ketones, aromatic rings, halogens, and terpenes.

2.2.3. Magnetometry

Figure 4a shows M vs. H curves of the samples 50GS-MNPs-Fe, 50MW-MNPs-Fe, and 50CO-MNPs-Fe at different temperatures (60 K, 62 K, 65 K, and 300 K). The zoom at 300 K (upper left box) indicates almost zero remanent magnetization (M_r), as well as a coercivity (H_c) close to zero in all samples. The zoom at 60 K (lower right box) indicates higher M_r and H_c in the 50MW-MNPs-Fe and 50CO-MNPs-Fe samples. Nonetheless, the M_r and H_c of the 50GS-MNPs-Fe sample remain close to zero. This behavior

and the Langevin-type curves suggest that at 300 K, all the samples exhibit an SPM behavior, and by reducing the temperature to 62 K and 65 K in the 50CO-MNPs-Fe and 50MW-MNPs-Fe samples, respectively, cross the blocking temperature (T_B) to a blocked state. Even so, the 50GS-MNPs-Fe sample maintains its SPM behavior, where the magnetic phase corresponded to 4.05 g of magnetite and maghemite in the sample and the rest (9.35 g) to the coating of organic molecules. Figure 4b indicates that reducing the temperature in the 50CO-MNPs-Fe and 50MW-MNPs-Fe samples increases H_c , indicating the opening of the M vs. H magnetization curves, which generates hysteresis. In contrast, in the 50GS-MNPs-Fe sample, the M vs. H curve remains close with SPM behavior.

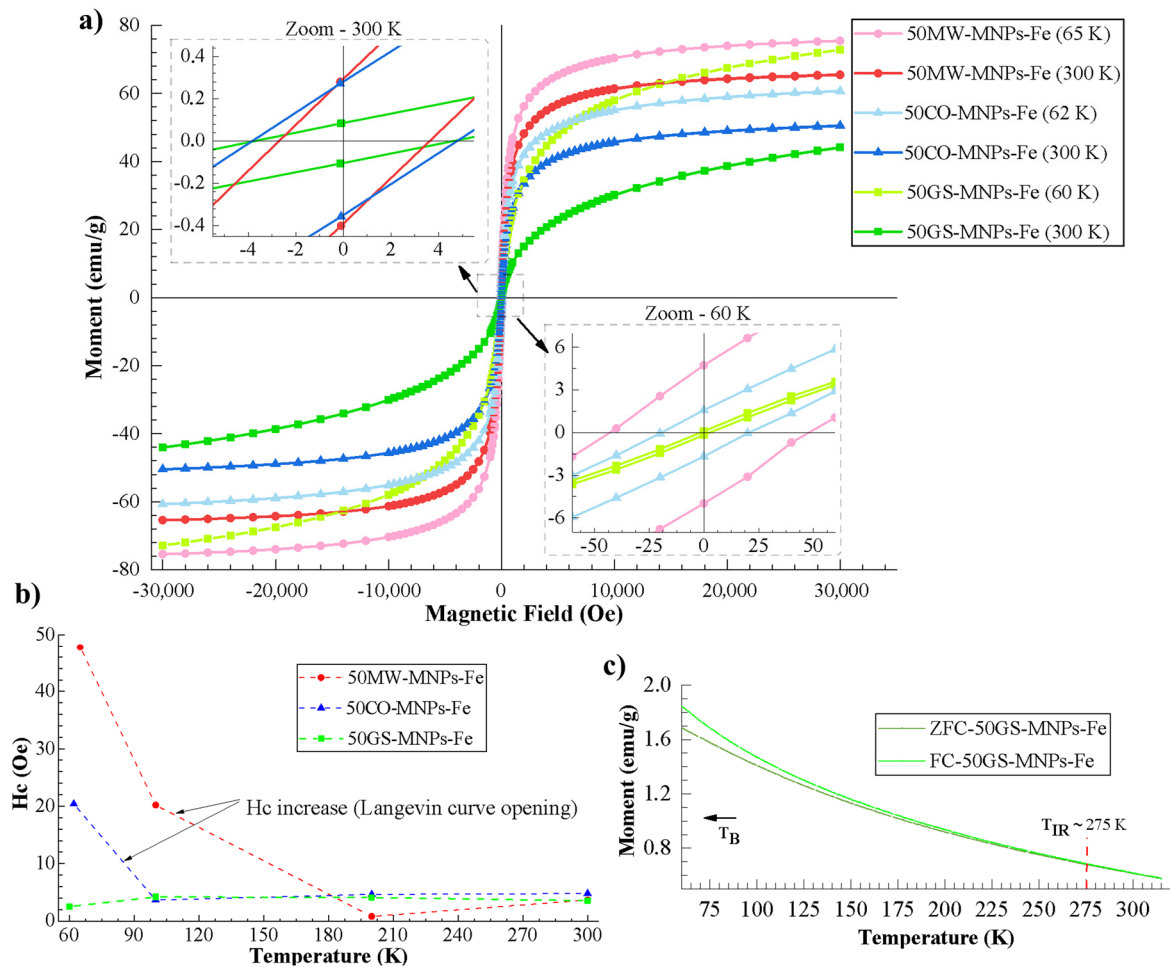


Figure 4. (a) M vs. H curves of the samples 50GS-MNPs-Fe, 50MW-MNPs-Fe, and 50CO-MNPs-Fe at different temperatures (60, 62, 65 and 300 K), (b) H_c vs. temperature curves of 50GS-MNPs-Fe, 50MW-MNPs-Fe, and 50CO-MNPs-Fe samples, (c) ZFC/FC curves of 50GS-MNPs-Fe sample.

The M_s of the 50MW-MNPs-Fe sample is the highest, being $65 \text{ emu} \cdot \text{g}^{-1}$ at 300 K and $75.4 \text{ emu} \cdot \text{g}^{-1}$ at 65.5 K, followed by the values of the 50CO-MNPs-Fe sample ($50.5 \text{ emu} \cdot \text{g}^{-1}$ at 300 K, $60.7 \text{ emu} \cdot \text{g}^{-1}$ at 62 K), and finally those from the 50GS-MNPs-Fe sample with a M_s of $44.1 \text{ emu} \cdot \text{g}^{-1}$ at 300 K and $72.8 \text{ emu} \cdot \text{g}^{-1}$ at 60 K. This result can be explained due to the 50MW-MNPs-Fe sample having the greatest magnetite phase (91.2%) as observed in XRD, followed by the 50CO-MNPs-Fe sample (63.5%) and then by the 50GS-MNPs-Fe sample (47.0%), which is consistent with the reported M_s of magnetite in the bulk state ($90\text{--}92 \text{ emu} \cdot \text{g}^{-1}$ at 300 K) [89–91] and maghemite ($30\text{--}80 \text{ emu} \cdot \text{g}^{-1}$ at 300 K) [92,93]. This reduction in M_s is also affected by the greater surface anisotropy (nanometric scale). Even so, it should be noted that the M_s of the 50GS-MNPs-Fe presented a significant increase at 60 K because the SPM behavior was maintained (see Figure 4a). It is also important to note that MNPs-Fe with several coherent diffracting crystalline domains (suggested by D_c in

XRD) reached monodomain magnetic (SPM) status. This can occur due to the energetic ease of aligning the atomic magnetic moments in the synthesized MNPs-Fe of sizes around 49.3 nm, generating a maximum net magnetic moment for each nanoparticle.

Figure 4c presents the ZFC and FC curves of the 50GS-MNPs-Fe sample and indicates that the temperature of T_B (transition from an SPM state to a blocked state) is below 60 K since no inflection is observed in the ZFC curve (operating capacity of the VSM), taking the criterion that the maximum peak of the ZFC curve corresponds to T_B [94]. The irreversibility temperature (T_{ir}) identified at 275 K (superposition of ZFC and FC curves) suggests a broad size distribution of the 50GS-MNPs-Fe [95], which is consistent with the presence of aggregates in the samples. The T_B of the 50MW-MNPs-Fe and 50CO-MNPs-Fe samples were determined at 211.1 K and 160.09 K, respectively. See Figure S6 for more information. Therefore, the 50GS-MNPs-Fe with SPM behavior can be used in applications that occur at temperatures greater than 60 K and below the Curie temperature; it must also be added that the terpenes, aldehydes, and other organic molecules (coating around 25 nm) prevent the aggregation of the 50GS-MNPs-Fe with a size of ~ 49.3 nm, quasi-spherical, with a magnetic nucleus (magnetite and maghemite), which improves its performance in bioapplications.

2.3. Cell Viability in ATCC RAW 264.7 Cells

Figure 5a,b show the ATCC RAW 264.7 cell viability percentage under different concentrations ($3.9\text{--}2000\ \mu\text{g}\cdot\text{mL}^{-1}$) of MNPs-Fe (50GS-MNPs, 50MW-MNPs-Fe, and 50CO-MNPs-Fe) for 24 h and 8 days, respectively.

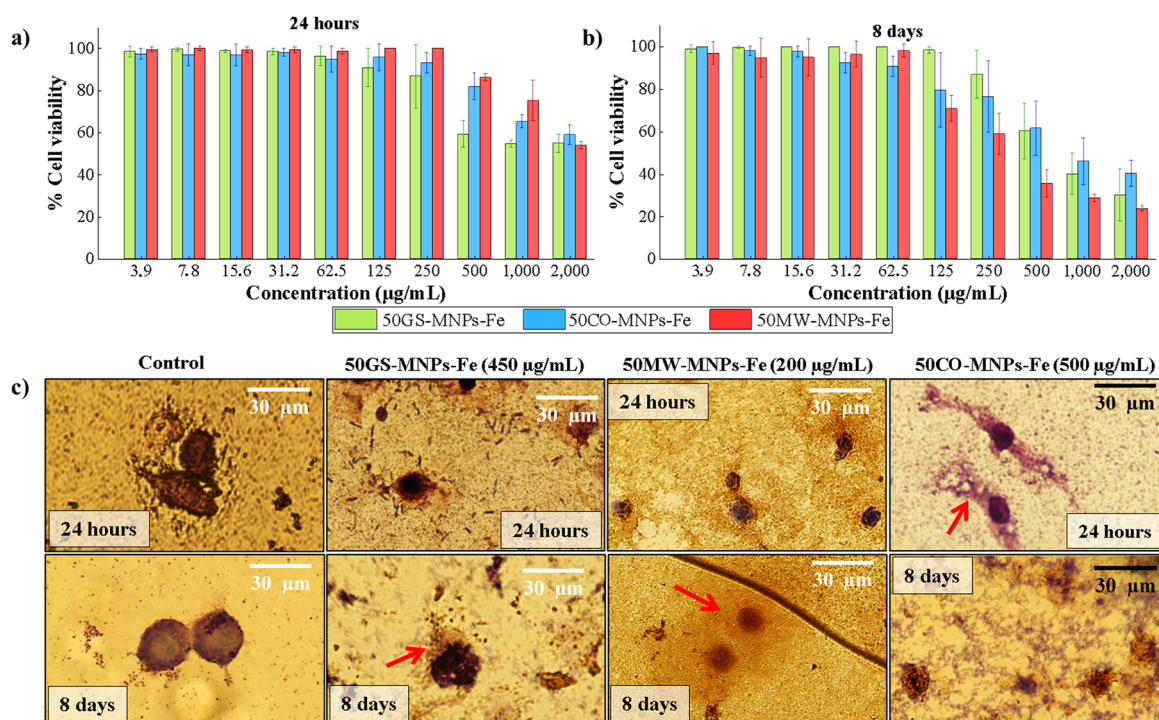


Figure 5. (a,b) Cell viability percentage in ATCC RAW 264.7 cells by Resazurin cell viability assay, using 50GS-MNPs-Fe, 50MW-MNPs-Fe, and 50CO-MNPs-Fe in $3.9\text{--}2000\ \mu\text{g}\cdot\text{mL}^{-1}$ concentrations for (a) 24 h and (b) 8 days, (c) Images obtained with the confocal microscope of ATCC RAW 264.7 cells incubated with 50GS-MNPs-Fe, 50MW-MNPs-Fe, and 50CO-MNPs-Fe to $450\ \mu\text{g}\cdot\text{mL}^{-1}$, $200\ \mu\text{g}\cdot\text{mL}^{-1}$, and $500\ \mu\text{g}\cdot\text{mL}^{-1}$, respectively, at 24 h and 8 days. All images are at $10\times$ magnification. The standard errors for IC₅₀ for 24 h are 5.992, 4.361, 3.368 $\mu\text{g}\cdot\text{mL}^{-1}$ for 50GS-MNPs-Fe, 50CO-MNPs-Fe, and 50MW-MNPs-Fe, respectively (see Table S6a), and for 48 h they are 6.855, 8.898 and 6.555 $\mu\text{g}\cdot\text{mL}^{-1}$ for 50MW-MNPs-Fe, 50CO-MNPs-Fe and 50GS-MNPs-Fe, respectively (see Table S6b).

The percentage of cell viability of ATCC RAW 264.7 cells under concentrations up to $250 \mu\text{g}\cdot\text{mL}^{-1}$ of MNPs-Fe (GS, MW, and CO) did not present significant changes at 24 h. The prolonged cell viability assays (8 days) allowed us to corroborate the biocompatibility of the MNPs-Fe [96–98], up to concentrations between 62.5 and $250 \mu\text{g}\cdot\text{mL}^{-1}$ of MNPs-Fe. The IC₅₀ (inhibition of 50% of the cells) obtained at 8 days with the samples 50GSMNPs-Fe, 50MW-MNPs-Fe, and 50CO-MNPs-Fe was $461.4 \mu\text{g}\cdot\text{mL}^{-1}$, $217.7 \mu\text{g}\cdot\text{mL}^{-1}$, and $520.2 \mu\text{g}\cdot\text{mL}^{-1}$, respectively, while at 24 h, IC₅₀ values of $318 \mu\text{g}\cdot\text{mL}^{-1}$, $1274 \mu\text{g}\cdot\text{mL}^{-1}$, and $601.6 \mu\text{g}\cdot\text{mL}^{-1}$ were obtained with the 50GSMNPs-Fe, 50MW-MNPs-Fe, and 50CO-MNPs-Fe samples, respectively. IC₅₀ was calculated in GraphPad Prism software with a 95% confidence interval and a four-parameter logistic fit (nonlinear least squares regression).

The cell viability of ATCC RAW 264.7 cells under concentrations up to $250 \mu\text{g}\cdot\text{mL}^{-1}$ of MNPs-Fe (GS, MW, and CO) did not present significant changes (80–100%) at 24 h. In contrast, after 8 days, the 50MW-MNPs-Fe and 50CO-MNPs-Fe samples did not show significant differences in cell viability (80–100%) for concentrations lower than $62.8 \mu\text{g}\cdot\text{mL}^{-1}$, while the 50GS-MNPs-Fe was maintained at $250 \mu\text{g}\cdot\text{mL}^{-1}$ (80–100% cell viability). This result is consistent with other studies with low concentrations (100 – $300 \mu\text{g}\cdot\text{mL}^{-1}$) of MNPs-Fe [99,100], where negligible cytotoxicity is reported.

These data can be confusing. However, these results can be elucidated by considering the state of the aqueous solutions studied by DLS (see Figure S7). The 50MW-MNPs-Fe sample presents more aggregates (~ 228.4 nm, ~ 1033 nm), followed by the 50CO-MNPs-Fe sample (~ 166.2 nm, ~ 726.2 nm). Therefore, the number of MNPs-Fe dispersed and available for internalization in the ATCC RAW 264.7 cells is reduced, which leads to less cytotoxicity. Thus, in 24 h, the 50GS-MNPs-Fe sample is apparently more cytotoxic. Still, in reality, we could say that they are better dispersed with fewer aggregates in such a way that there are more MNPs-Fe internalized in the macrophage cells, causing oxidative stress. Then, as the test days go by (day 2, day 3, etc., until day 8), the naked 50MW-MNPs-Fe and 50CO-MNPs-Fe samples (only with magnetite and maghemite phases identified by XRD, without organic coating) degrade as a source of Fe^{+2} and Fe^{+3} ions towards the cell culture medium. These ions are highly reactive and cause oxidative stress and, therefore, more significant cytotoxicity. This result explains the dramatic change in IC₅₀ at 24 h and 8 days in 50MW-MNPs-Fe. In samples with 50GS-MNPs-Fe, those mentioned above can also occur, but to a lesser extent; that is, the organic coating prevents their aggregation (aggregates up to ~ 224.8 nm), as observed in DLS Figure S7. This agrees with the work of Guldris et al. [101], who used MNPs-Fe functionalized with poly(acrylic acid) and MSCs (mesenchymal stem cells), which maintain viability for 12 days.

These results suggested that in short periods (24 h), 50MW-MNPs-Fe and 50CO-MNPs-Fe have lower cytotoxicity. That is, 50% of ATCC RAW 264.7 cells maintained their normal mitochondrial metabolic function at around 1274 and $601.6 \mu\text{g}\cdot\text{mL}^{-1}$ concentrations for 50MW-MNPs-Fe and 50CO-MNPs-Fe, respectively. In contrast, the 50GS-MNPs-Fe sample achieved an IC₅₀ of $318.2 \mu\text{g}\cdot\text{mL}^{-1}$. That is, a lower concentration of MNPs-Fe caused more significant cell death. In more prolonged periods (8 days), the IC₅₀ induced by the 50GS-MNPs-Fe and 50CO-MNPs-Fe samples were higher (461.4 and $520.2 \mu\text{g}\cdot\text{mL}^{-1}$), while the 50MW-MNPs-Fe samples were more cytotoxic. ($217.7 \mu\text{g}\cdot\text{mL}^{-1}$).

Figure 5c presents images taken with a confocal microscope of the Giemsa staining assay, with ATCC RAW 264.7 cells at concentrations of $450 \mu\text{g}\cdot\text{mL}^{-1}$, $200 \mu\text{g}\cdot\text{mL}^{-1}$, and $500 \mu\text{g}\cdot\text{mL}^{-1}$ of 50GS-MNPs-Fe, 50MW-MNPs-Fe, and 50CO-MNPs-Fe samples, respectively. The concentrations in the Giemsa staining assay were approximated to the IC₅₀ calculated at 8 days in the Resazurin cell viability assay. The Giemsa staining assay enabled the study of the damage and changes produced by MNPs-Fe in ATCC RAW 264.7 cells. At 24 h, the 50GS-MNPs-Fe sample reduced the size of the ATCC RAW 264.7 cells compared to the control. At 8 days, a cell size like that of the control was observed, as well as a small leak of the cytoplasm (red arrow). At 24 h and 8 days, chromatin condensation was observed without significant changes in the morphology of the cell membrane, which indicates

death by apoptosis. A lack of nutrients or excess ROS can cause this programmed cell death. ROS can induce mitoptosis death, which arises from removing ROS-overproducing mitochondria by autophagy [102].

In contrast, the samples with 50MW-MNPs-Fe induced a reduction in cell size and significant cytoplasm leakage after 24 h and 8 days. Likewise, the 50CO-MNPs-Fe samples caused severe damage to the cell membrane and the leakage of the cytoplasmic elements (red arrows). Both types of MNPs-Fe (CO and MW) produced a necrosis-like death, a more aggressive and uncontrolled death.

Thus, 50GS-MNPs-Fe presents advantages over those obtained by CO and MW in terms of biocompatibility since the organic molecules of the orange peel prevent their aggregation and induce cell death by apoptosis in higher concentrations.

2.4. Photothermal Studies

Figure 6 depicts the photothermal study of aqueous solutions with 50GS-MNPs-Fe, 50MW-MNPs-Fe, and 50CO-MNPs-Fe at concentrations of $8 \text{ mg}\cdot\text{mL}^{-1}$, including the control sample of DI water. All samples (in triplicate) were irradiated under the red light of 630 nm and $65.5 \text{ mW}\cdot\text{cm}^{-2}$ from an LED source. On the horizontal axis of Figure 6, the doses of light supplied are linked according to the irradiation times (increments of two minutes) with a total of 44 min of irradiation. All the MNPs-Fe solutions indicated that the temperature reaches a temperature threshold of 30 min. The 50GS-MNPs-Fe, 50MW-MNPs-Fe, and 50CO-MNPs-Fe reached maximum temperatures of $50.8 \pm 0.2 \text{ }^\circ\text{C}$, $51.7 \pm 0.6 \text{ }^\circ\text{C}$, and $49.6 \pm 0.71 \text{ }^\circ\text{C}$, respectively, while the control sample (DI water) reached $42.3 \pm 0.1 \text{ }^\circ\text{C}$. The photothermal effect was due to this type of nanoparticle LSPR [53]. These results indicate that all samples are suitable PTAs in the PTT for eliminating bacterial and/or tumor cells [17,55,103–107].

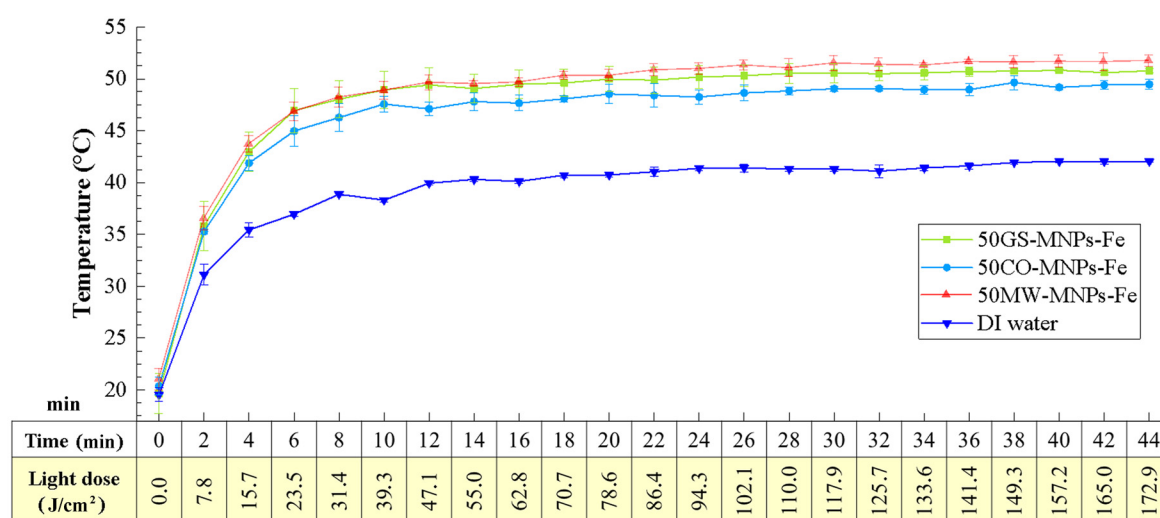


Figure 6. Thermal study of aqueous solutions with 50GS-MNPs-Fe, 50MW-MNPs-Fe, and 50CO-MNPs-Fe samples at concentrations of $8 \text{ mg}\cdot\text{mL}^{-1}$ and the control sample of DI water with red light irradiation at 630 nm and $65.5 \text{ mW}\cdot\text{cm}^{-2}$ from an LED source.

It is essential to highlight that the 50GS-MNPs-Fe sample achieved a photothermal effect similar to MW and CO, despite having a lower amount of magnetite and maghemite phase. The concentrations for this study were obtained with the weight obtained after the synthesis.

2.5. Antibacterial PTT

Figure 7a,b show the Log_{10} (CFU) count of the spread plate assays in *S. aureus* and *E. coli* bacteria, respectively. All groups were treated with MNPs-Fe (GS, MW, and CO) using a concentration of $8 \text{ mg}\cdot\text{mL}^{-1}$ of MNPs-Fe in PBS. The antibacterial activity of

50GS-MNPs-Fe against *S. aureus* without irradiation is small in 0.25 Log₁₀ (CFU). Likewise, 50MW-MNPs-Fe and 50CO-MNPs-Fe without irradiation did not have significant antibacterial activity. Irradiation with a red light at 630 nm (65.5 mW·cm⁻²) for 30 min towards *S. aureus* (without MNPs-Fe) had no antibacterial effect. However, 50GS-MNPs-Fe and 50CO-MNPs-Fe with red light irradiation at 630 nm (65.5 mW·cm⁻²) for 30 min completely inhibited *S. aureus* bacteria. The 50MW-MNPs-Fe with red light irradiation at 630 nm (65.5 mW·cm⁻², 30 min) inhibited 3.99 Log (CFU) of *S. aureus*.

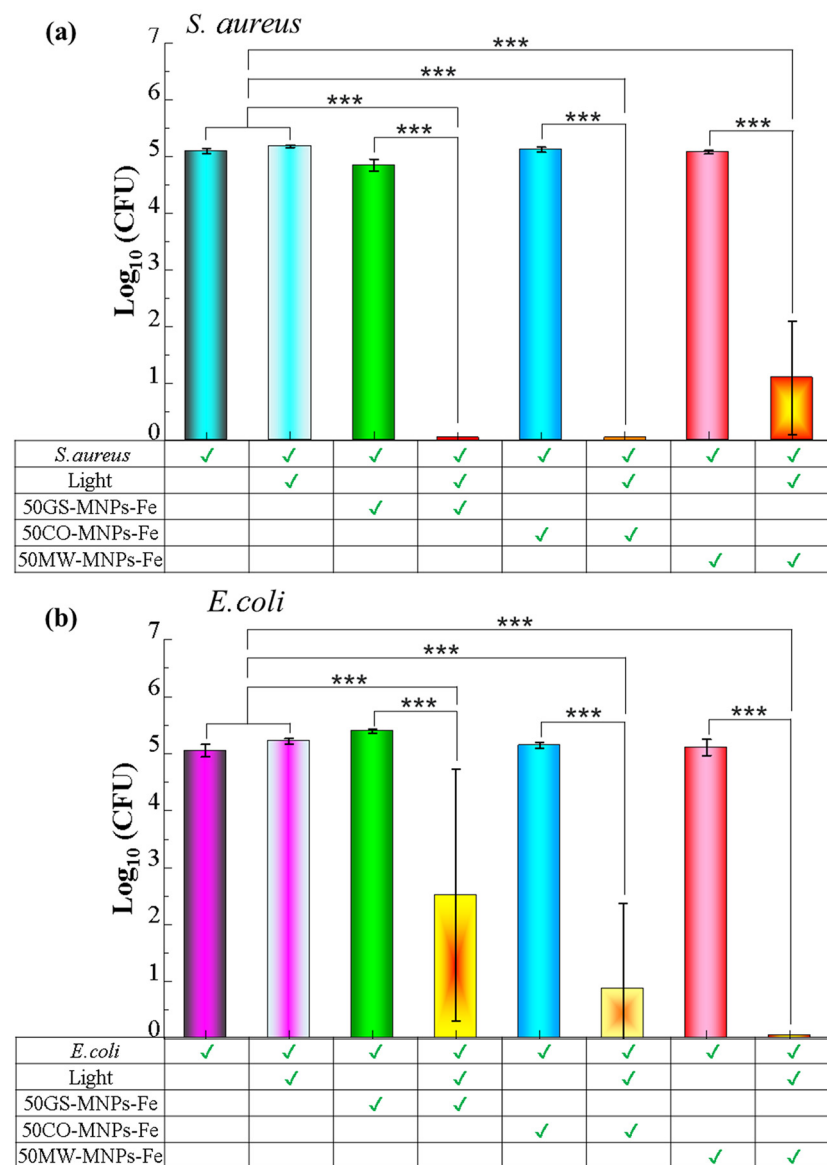


Figure 7. Counting of Log₁₀ (CFU) in the spread plate assay to groups; [Bacteria], [Bacteria + Light], [Bacteria + MNPs-Fe (GS, MW, CO)], and [Bacteria + MNPs-Fe (GS, MW, CO) + light], in (a) *S. aureus* y (b) *E. coli*. Significant differences in means according to the Tukey test (***) $p \leq 0.001$) based in Table S5a–c.

The antibacterial activity of all MNPs-Fe (GS, MW, and CO) against *E. coli* is negligible. The 50MW-MNPs-Fe irradiated with a red light at 630 nm (65.5 mW·cm⁻², 30 min) completely inhibited *E. coli*, while the 50GS-MNPs-Fe and 50CO-MNPs-Fe were able to inhibit 2.54 Log₁₀ (CFU) and 4.19 Log₁₀ (CFU), respectively (see Figure 8b for 50GS-MNPs-Fe against *E. coli*). The results indicated that 50GS-MNPs-Fe and 50CO-MNPs-Fe have excellent antibacterial activity against *S. aureus* (Gram positive) (see Figures 7a and 8a),

while 50MW-MNPs-Fe are capable of inhibiting Gram-negative bacteria as *E. coli*; see Figures 7b and 8c.

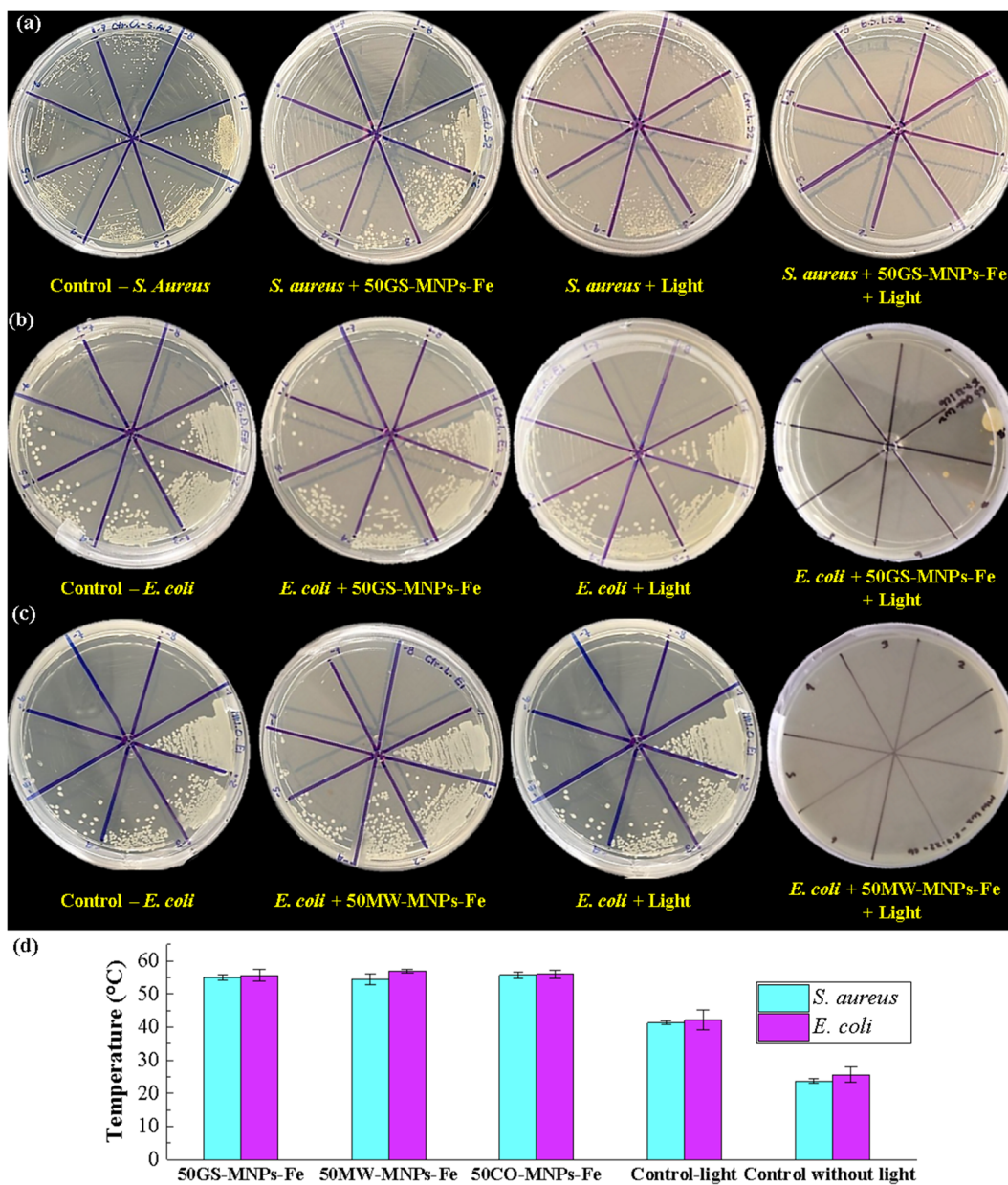


Figure 8. Images of the spread plate assay of the groups: (a) [Control-*S. aureus*], [*S. aureus* + 50GS-MNPs-Fe], [*S. aureus* + Light], [*S. aureus* + 50GS-MNPs-Fe + Light], (b) [Control-*E. coli*], [*E. coli* + 50GS-MNPs-Fe], [*E. coli* + Light], [*E. coli* + 50GS-MNPs-Fe + Light], (c) [Control-*E. coli*], [*E. coli* + 50MW-MNPs-Fe], [*E. coli* + Light], [*E. coli* + 50MW-MNPs-Fe + Light], (d) Temperatures reached in antibacterial PTT after irradiation with 117.9 J·cm⁻² and control without irradiation.

The photothermal effect of the MNPs-Fe contributed to bacterial elimination. However, it is highlighted that in laser irradiation, MNPs-Fe act as a photosensitizing agent (PS) that increases the generation of ROS (singlet oxygen, etc.), which causes oxidative stress and cell death. Therefore, bacteria inhibition is due to the contribution of the photothermal effect along with ROS generation that produces a photodynamic effect, as proposed in several studies [21,108–110].

Figure 8b shows that the final temperature after the irradiation (antibacterial PTT) was higher than 50 °C for both bacterial strains, while the controls of light (bacteria + light)

reached temperatures around 40 °C. In all the irradiated cases, the dose of light supplied corresponds to 117.9 J·cm⁻².

The results of the antibacterial activity indicate that the 50GS-MNPs-Fe inhibit *S. aureus* and partially *E. coli*, which is in accordance with [71]. However, the concentrations of MNPs-Fe used in our studies are higher, reaching temperatures of ~50 °C in antibacterial PTT, similar to those reported by Qing G. et al. [111] from 43 to 49 °C (with 808 nm, 0.5 W·cm⁻²).

3. Materials and Methods

3.1. Materials

Iron III chloride hexahydrate (FeCl₃·6H₂O) was from Mallinckrodt Chemical Ltd. (Chesterfield, UK). Iron II sulfate heptahydrate (FeSO₄·7H₂O) was from MERCK (Rahway, NJ, USA). Ammonium hydroxide (NH₄OH) was from BDH Chemicals (Welch, WV, USA). DMEM-Dulbecco's Modified Eagle Medium, agar, and broth culture was from Fisher Scientific (Princeton, NJ, USA). Resazurin sodium salt was from Sigma Aldrich (St. Louis, MO, USA). Giemsa Stain was from MERK (RJ, Brazil). No further purification was performed on the chemical agents.

3.2. Preparation of Orange Peel Extract

First, the endocarp and inner mesocarp were removed from the orange waste to obtain only the orange peel (outer mesocarp). Then, small pieces approximately 1 × 2 cm in size were obtained. A total of 25 g of orange peel was weighed and thoroughly washed using deionized (DI) water. The orange peel and 250 mL of DI water were blended using a domestic blender at 2000 rpm for 10 min (Oster-4172, 375 W, Acuña, Mexico). The mixture was irradiated in a domestic MW oven (General Electric, JES-700 W, Boston, MA, USA) for 5 min. Finally, the mixture was cooled and sieved using paper filters (Brew Rite, Little Chute, WI, USA). The vegetal extract was used within the next 30 min.

3.3. GS of MNPs-Fe

FeCl₃·6H₂O (210 mg) and FeSO₄·7 H₂O (105 mg) were dissolved in 10 mL DI water in a beaker at 70 °C with continuous magnetic stirring. Then, several mixtures of 25 mL of orange peel extract with NH₄OH were prepared in different volume percentages: 100%, 75%, 50%, 25%, and 0% NH₄OH. A solution of FeCl₃·6H₂O and FeSO₄·7H₂O was added to each mixture of orange peel extract and NH₄OH and subsequently irradiated with MW (General Electric, JES-70W) for three intervals of 30 s. The black appearance indicated the formation MNPs-Fe, which were washed with DI water and under a magnetic field to remove phytochemicals excess and non-magnetic particles. The MNPs-Fe obtained with 100%, 75%, 50%, 25%, and 0% of NH₄OH are called 100GS-MNPs-Fe, 75GS-MNPs-Fe, 50GS-MNPs-Fe, 25GS-MNPs-Fe, and 0GS-MNPs-Fe, respectively.

To compare the produced weight of the GS, cytotoxicity, antibacterial activity, and magnetic properties such as saturation magnetization (M_s) and blocking temperature (T_B), MNPs-Fe were prepared by CO and MW routes without orange peel extract. In the case of CO synthesis, a procedure similar to that described in [112–114] was followed, using FeCl₃·6H₂O (210 mg) and FeSO₄·7 H₂O (105 mg) as precursors with the identical aliquots used in GS. Mixtures according to the percentages used in the GS were prepared with DI water and NH₄OH. Then, the temperature was raised to 80 °C on a hot plate. Later, the solution of precursor salts was added drop by drop. Magnetic stirring was maintained for 1 h, and then the NPs were washed with DI water and a permanent magnet. The MW synthesis followed the same procedure as the GS [31,115], replacing the orange peel extract with DI water. The samples obtained by CO with 100%, 75%, 50%, and 25% of NH₄OH (volume) were called 100CO-MNPs-Fe, 75CO-MNPs-Fe, 50CO-MNPs-Fe, and 25CO-MNPs-Fe, respectively. The samples obtained by MW synthesis were denominated as 100MW-MNPs-Fe, 75MW-MNPs-Fe, 50MW-MNPs-Fe, and 25MW-MNPs-Fe, according to the percentage of NH₄OH used.

In the different tests, samples of MNPs-Fe were in aqueous dispersions and powder form (dry). In the case of MNPs-Fe powder, drying was carried out in an oven at 40 °C for 42 h.

3.4. MNPs-Fe Characterization

The morphology and size distribution of the MNPs-Fe were studied by scanning electron microscopy (SEM) in a Tescan Mira 3 microscope (Tescan, Brno, Czech Republic) equipped with a Schottky field emission source at 25 kV (JEOL Ltd., Tokyo, Japan). For this, an aliquot of MNPs-Fe was dispersed in 1 mL of DI water and then dried on a sample holder at room temperature. To measure the hydrodynamic diameter of the MNPs-Fe, a dynamic light scattering (DLS) analysis was performed in a Particle Size Analyzer 90Plus-11554 (Brookhaven Instruments Corporation, Suffolk, NY, USA). Thus, 5 mL of dispersion was used for the sample of MNPs-Fe in DI water at 1 mg·mL⁻¹. The topography of MNPs-Fe was studied by atomic force microscopy (AFM) in a Dimension Icon Atomic Force Microscope (Bruker, Billerica, MA, USA), in Tapping Mode with a scanning range of 90 μm × 90 μm (XY) and 10 μm (Z) equipped with a Dim 4000 type scanner. An aliquot of MNPs-Fe on DI water was used at 10 mg·mL⁻¹.

The elemental composition was determined by energy dispersive X-ray spectroscopy (EDS) in the same Tescan Mira 3 microscope using a detector Xflash[®] 6–30 (Bruker, Billerica, MA, USA), with a resolution of 123 eV in Mn K α . The crystalline structure and phases of iron oxide in the MNPs-Fe were identified by X-ray diffraction (XRD) in an Empyrean diffractometer (Malvern Panalytical, Malvern, UK) equipped with a copper X-ray tube (Empyrean Cu LFF, Almelo, Netherlands) and Cu-K α radiation at $2\theta = 5\text{--}90^\circ$ with 45 kV and 40 mA. For this, 93.3–434 mg of MNPs-Fe powder was used. Fourier transform infrared (FTIR) and Raman spectroscopy allowed the study of the molecular vibrations of MNPs-Fe. FTIR spectra were acquired using a Spectrum 100 (86660) spectrometer (Perkin Elmer, Waltham, MA, USA) equipped with a Spotlight 200 N/S 86672 microscope with an analysis range of 500–4000 cm⁻¹ and 5 mg of MNPs-Fe powder. Raman spectra were recorded using a LabRAM HR Evolution spectrometer (HORIBA Corporation, Kyoto, Japan) with an analysis range between 100 and 2000 cm⁻¹ and a sensitivity of 10 cm⁻¹. For this, 5 mg of MNPs-Fe were dispersed in 5 mL of DI water, and an aliquot was dried on a glass slide at room temperature.

The magnetic behavior of MNPs-Fe was analyzed in a Quantum Design Versalab Vibrating Sample Magnetometer (VSM) (Quantum Design, San Diego, CA, USA) with an operating range of –3 to 3 Tesla (–30 to 30 kOe) and 50–400 K with sensitivity $\sim 1 \times 10^{-6}$ emu. Thus, this generated two types of curves: magnetization (M) as a function of the external magnetic field (H) at a constant temperature and magnetization (M) as a function of temperature (cooling from 315 K to 60 K) in the presence of zero magnetic fields (zero field cooling, ZFC curves) and with the presence of a small magnetic field of 50 Oe (field cooling, FC curves).

3.5. Cytotoxicity Assay

Cytotoxicity assays measure the rate of proliferation and the toxic effects on the cell when using certain materials, such as MNPs-Fe. Particularly, this cytotoxicity study used as a test subject, an animal cell line ATCC RAW 264.7 of the macrophage type from mice (*Mus musculus*), donated by CISEAL.

3.5.1. Cell Culture

The animal cell line ATCC RAW 264.7 remained in DMEM-Dulbecco's Modified Eagle Medium accompaniment with 1% penicillin/streptomycin and fetal bovine serum (FBS)–10% (DMEM-10) in a Series II Water Jacket–CO₂ Incubator (Thermo Scientific, Hillsboro, OR, USA), at 37 °C in an atmosphere of CO₂ 5% and 98% relative humidity (RH) for 24 h.

3.5.2. Resazurin Cell Viability Assay

Within a 96-well plate with a black background, 2×10^4 cells/well were seeded using 100 μL of DMEM-10 (incubated at 37°C) with an atmosphere of 5% CO_2 and 98% of RH for 24 h. MNPs-Fe were diluted in 10-fold serial dilutions (2000, 1000, 500, 250, 125, 62.5, 31.2, 15.6, 7.8, and $3.9 \mu\text{g}\cdot\text{mL}^{-1}$) with DMEM-10. They were then placed in the seeded cells, maintaining the respective life control wells. Thus, 10 μL of resazurin sodium salt at 3 mM in PBS per well was added, and the plate was incubated for 24 h. Finally, fluorescence was measured at 520, 580, and 640 nm excitation on a GloMax (Promega, Madison, WI, USA) multimodal microplate reader. In viable cells with adequate mitochondrial metabolic function, redox reactions occurred between the mitochondrial coenzymes nicotinamide adenine dinucleotide NADH (reduced form) and its oxidized NAD^+ , irreversibly reducing resazurin to resorufin. The resorufin fluoresces at 560 nm, then is excreted to the culture medium, where it was quantified with a plate fluorometer, this signal being a function of the number of viable cells in the sample [116,117]. All samples were carried out in triplicate.

3.5.3. Giemsa Staining Assay

Three sterile circular coverslips per well were aseptically placed into two 6-well plates, and 5.5×10^5 ATCC RAW 264.7 cells per well were plated and incubated at 37°C with a 5% CO_2 atmosphere and 98% HR. The following day, cells were washed with PBS, and the MNPs-Fe were added and incubated. A coverslip was removed from each well at 24 h and 8 days, later fixed with 5% of glutaraldehyde for 24 h, and then immersed in Giemsa stain for 30 min. Finally, images were taken with a confocal microscope. This assay was carried out to stain the cell organelles and observe the damage caused by the presence of MNPs-Fe, such as cytoplasmic condensations, damage to the cell membrane, and so on.

3.6. Antibacterial Activity

Antibacterial activity studies used *S. aureus* ATCC 25923 and *E. coli* ATCC 25922 bacteria as test subjects (both donated by CISeAL). Light irradiation-assisted PTT was employed as an antibacterial strategy, which converts light energy into heat that kills bacterial cells by raising the local temperature.

3.6.1. Thermal Studies

The photothermal studies measured the temperature increase with a digital thermometer DET-306 (SCANMED, 0.1°C sensitivity) in MNPs-Fe solutions and DI water at $8 \text{ mg}\cdot\text{mL}^{-1}$ with red light irradiation of 630 nm from a $65.5 \text{ mW}\cdot\text{cm}^{-2}$ LED source. The temperature was registered every two minutes until its increase stopped. Three measurement runs were performed for each type of Fe-MNPs and the control.

3.6.2. Bacterial Culture

For bacterial culture, cryovials were provided with *S. aureus* and *E. coli* bacteria that were thawed at room temperature and inoculated in Muller Hinton Broth (Difco™, Princeton, NJ, USA) for incubation (SL Shel lab incubator–1525, San Diego, CA, USA) for 24 h at 37°C . The number of Colony-Forming Units (CFU) was established using a spectrophotometer (Thermo Scientific™ Orion™ AquaMate 8000 UV-Vis, Waltham, MA, USA) for absorbance of 0.2 OD and 0.4 OD, equivalent to 10^7 CFU·mL⁻¹ for *E. coli* and 10^6 CFU·mL⁻¹ for *S. aureus*, respectively.

3.6.3. Spread Plate Assay

Four groups were considered for each bacterium: (1) control (bacteria alone), (2) bacterium + light, (3) bacterium + MNPs-Fe, and (4) bacterium + MNPs-Fe + light. All assays were performed in triplicate. Consequently, 1 mL of bacterial culture (*E. coli* and *S. aureus*) was taken and centrifuged at 3,000 rpm for 10 min. Then, the supernatant was discarded, and 1 mL of MNPs-Fe dispersed in PBS was added ($8 \text{ mg}\cdot\text{mL}^{-1}$) or PBS according to the test groups and homogenized with vortex. Each sample was incubated

in the dark for 25 min at 37 °C. Then, bacteria + light and bacteria + MNPs-Fe + light groups were irradiated with red light (630 nm) in a LED source of 65.5 mW·cm⁻² for 30 min. Later, an aliquot of 0.5 mL of each sample was taken to eight serial dilutions (1:2 to 1:256) in PBS to inoculate 4 µL of each dilution into a divided eight-parts Petri dish with Muller Hinton Agar (Difco™) spread. Finally, the Petri dishes were incubated at 37 °C for 24 h to count the CFU. The temperature reached in the PTT was measured with a digital thermometer DET-306 as soon as the laser irradiation was suspended. Likewise, in a control without irradiation, the temperature was recorded at the end of the incubation time with the MNPs-Fe.

4. Conclusions

In this work, MNPs-Fe were synthesized by an environmentally friendly approach using orange residues. These MNPs-Fe were physicochemically and magnetically characterized. The results showed the morphology of nano-spheres coated with organic molecules (from the orange peel). The MNPs-Fe presented crystalline phases of magnetite and maghemite. In addition, an SPM behavior was identified. The GS-MNPs-Fe were compared with others synthesized through CO and MW to study the influence of NH₄OH on the produced weights of MNPs-Fe. Thus, the minimum aliquot of NH₄OH was selected (50% v/v) to maintain an adequate produced weight (29.3% mass yield) of GS (sample 50GS-MNPs-Fe). Photothermal studies indicated that 50GS-MNPs-Fe reached a photothermal effect similar to those obtained by MW and CO (~50 °C), indicating that the organic molecules did not affect light conversion into heat. Cytotoxicity studies reflected low toxicity of all the MNPs-Fe for concentrations lower than 250 µg/mL, with an improvement in the viability of the macrophages at 8 days with 50GS-MNPs-Fe. Likewise, the 50GS-MNPs-Fe sample inhibited *S. aureus*, but not wholly *E. coli*, since Gram-negative bacteria have a robust bacterial wall structure (lipopolysaccharides, peptidoglycan, and phospholipids). These results indicate that 50GS-MNPs-Fe are suitable candidates as broad-spectrum PTAs in antibacterial PTT, MRI, and magnetic hyperthermia.

Supplementary Materials: The following supporting information can be downloaded at: <https://www.mdpi.com/article/10.3390/ijms24054770/s1>.

Author Contributions: Conceptualization, M.P.R.; Methodology, M.J.B.; Validation, D.G.G. and M.J.B.; Formal analysis, D.G.G., M.A.S., K.J.L., K.O.C., A.D., K.V. and D.N.; Investigation, D.G.G. and C.G.-R.; Writing—original draft, D.G.G.; Writing—review & editing, K.J.L.; Supervision, M.R.R. and M.P.R.; Project administration, M.P.R.; Funding acquisition, M.R.R. and M.P.R. All authors have read and agreed to the published version of the manuscript.

Funding: Project PIIF-20-05 National Polytechnic School and Project 089-UIO-2021 Pontifical Catholic University of Ecuador. Funding acquisition, Miryan Rosita Rivera-PUCE (Pontificia Universidad Católica del Ecuador), and María Paulina ROMERO-EPN (Escuela Politécnica Nacional, Quito-Ecuador).

Informed Consent Statement: Not applicable.

Data Availability Statement: Additional results found in this work are presented in Supplementary Materials, which will be attached to this document.

Acknowledgments: The authors thank Jaime Costales for the donation of the ATCC RAW 264.7 cell line.

Conflicts of Interest: The authors declare no conflict of interest.

References

1. Wang, L.; Hu, C. The antimicrobial activity of nanoparticles: Present situation and prospects for the future. *Int. J. Nanomed.* **2017**, *12*, 1227–1249. [[CrossRef](#)] [[PubMed](#)]
2. Kong, X.; Liu, X.; Zheng, Y.; Chu, P.K.; Zhang, Y.; Wu, S. Graphitic carbon nitride-based materials for photocatalytic antibacterial application. *Mater. Sci. Eng. R Rep.* **2021**, *145*, 100610. [[CrossRef](#)]
3. Liang, J.; Li, W.; Chen, J.; Huang, X.; Liu, Y.; Zhang, X.; Shu, W.; Lei, B.; Zhang, H. Antibacterial Activity and Synergetic Mechanism of Carbon Dots against Gram-Positive and Gram-Negative Bacteria. *ACS Appl. Bio Mater.* **2021**, *4*, 6937–6945. [[CrossRef](#)] [[PubMed](#)]

4. Rodrigues, G.R.; López-abarrategui, C.; De, I.; Gómez, S. Antimicrobial magnetic nanoparticles based-therapies for controlling infectious diseases. *Int. J. Pharm.* **2018**, *555*, 356–357. [[CrossRef](#)]
5. Paramanatham, P.; Anju, V.T.; Dyavaiah, M.; Siddhardha, B. Applications of Carbon-Based Nanomaterials for Antimicrobial Photodynamic Therapy. In *Nanotechnology in the Life Sciences*; Springer: Berlin/Heidelberg, Germany, 2019; pp. 237–259.
6. Feng, Y.; Liu, L.; Zhang, J.; Aslan, H.; Dong, M. Photoactive antimicrobial nanomaterials. *J. Mater. Chem. B* **2017**, *5*, 8631–8652. [[CrossRef](#)]
7. Smith, M. Antibiotic Resistance Mechanisms. In *Journeys in Medicine and Research on Three Continents over 50 Years*; ASM Journals: Ames, IA, USA, 2017; pp. 95–99. [[CrossRef](#)]
8. Potbhare, A.K.; Umekar, M.S.; Chouke, P.B.; Bagade, M.B.; Tarik Aziz, S.K.; Abdala, A.A.; Chaudhary, R.G. Bioinspired graphene-based silver nanoparticles: Fabrication, characterization and antibacterial activity. *Mater. Today Proc.* **2019**, *29*, 720–725. [[CrossRef](#)]
9. El-Gendy, N.S.; El-Gendy, N.S.; Omran, B.A. Green Synthesis of Nanoparticles for Water Treatment. In *Nano and Bio-Based Technologies for Wastewater Treatment*; Wiley: Hoboken, NJ, USA, 2019; pp. 205–263. [[CrossRef](#)]
10. Ajinkya, N.; Yu, X.; Kaithal, P.; Luo, H.; Somani, P. Magnetic iron oxide nanoparticle (IONP) synthesis to applications: Present and future. *Materials* **2020**, *13*, 4644. [[CrossRef](#)]
11. Xin, Q.; Shah, H.; Nawaz, A.; Xie, W.; Akram, M.Z.; Batool, A.; Tian, L.; Jan, S.U.; Boddula, R.; Guo, B.; et al. Antibacterial Carbon-Based Nanomaterials. *Adv. Mater.* **2019**, *31*, 1804838. [[CrossRef](#)]
12. Jalal, M.; Ansari, M.A.; Alzohairy, M.A.; Ali, S.G.; Khan, H.M.; Almatroudi, A.; Raees, K. Biosynthesis of silver nanoparticles from oropharyngeal *Candida glabrata* isolates and their antimicrobial activity against clinical strains of bacteria and fungi. *Nanomaterials* **2018**, *8*, 586. [[CrossRef](#)]
13. Rajendracharu, S.; Betül, K.C. The activation energy and antibacterial investigation of spherical Fe₃O₄ nanoparticles prepared by *Crocus sativus* (Saffron) flowers. *Biointerface Res. Appl. Chem. Open Access J.* **2020**, *10*, 5951–5959. [[CrossRef](#)]
14. Jaber, M.; Mushtaq, A.; Zhang, K.; Wu, J.; Luo, D.; Yi, Z.; Iqbal, M.Z.; Kong, X. Gram-scale synthesis of splat-shaped Ag-TiO₂ nanocomposites for enhanced antimicrobial properties. *Beilstein J. Nanotechnol.* **2020**, *11*, 1119–1125. [[CrossRef](#)] [[PubMed](#)]
15. Hou, Y.; Mushtaq, A.; Tang, Z.; Dempsey, E.; Wu, Y.; Lu, Y.; Tian, C.; Farheen, J.; Kong, X.; Iqbal, M.Z. ROS-responsive Ag-TiO₂ hybrid nanorods for enhanced photodynamic therapy of breast cancer and antimicrobial applications. *J. Sci. Adv. Mater. Devices* **2022**, *7*, 100417. [[CrossRef](#)]
16. Mushtaq, A.; Zhao, R.; Luo, D.; Dempsey, E.; Wang, X.; Iqbal, M.Z.; Kong, X. Magnetic hydroxyapatite nanocomposites: The advances from synthesis to biomedical applications. *Mater. Des.* **2021**, *197*, 109269. [[CrossRef](#)]
17. Jabir, M.S.; Nayef, U.M.; Kadhim, W.K.A. Polyethylene glycol-functionalized magnetic (Fe₃O₄) nanoparticles: A novel DNA-mediated antibacterial agent. *Nano Biomed. Eng.* **2019**, *11*, 18–27. [[CrossRef](#)]
18. Rummyantceva, V.; Rummyantceva, V.; Koshel, E.; Vinogradov, V. Biocide-conjugated magnetite nanoparticles as an advanced platform for biofilm treatment. *Ther. Deliv.* **2019**, *10*, 241–250. [[CrossRef](#)]
19. Ling, W.; Wang, M.; Xiong, C.; Xie, D.; Chen, Q.; Chu, X.; Qiu, X.; Li, Y.; Xiao, X. Synthesis, surface modification, and applications of magnetic iron oxide nanoparticles. *J. Mater. Res.* **2019**, *34*, 1828–1844. [[CrossRef](#)]
20. Chen, Y.; Gao, Y.; Chen, Y.; Liu, L.; Mo, A.; Peng, Q. Nanomaterials-based photothermal therapy and its potentials in antibacterial treatment. *J. Control. Release* **2020**, *328*, 251–262. [[CrossRef](#)]
21. Jędrzak, A.; Grześkowiak, B.F.; Golba, K.; Coy, E.; Synoradzki, K.; Jurga, S.; Jesionowski, T.; Mrówczyński, R. Magnetite nanoparticles and spheres for chemo-and photothermal therapy of hepatocellular carcinoma in vitro. *Int. J. Nanomed.* **2020**, *15*, 7923–7936. [[CrossRef](#)]
22. Songca, S.P.; Adjei, Y. Applications of Antimicrobial Photodynamic Therapy against Bacterial Biofilms. *Int. J. Mol. Sci.* **2022**, *23*, 3209. [[CrossRef](#)]
23. Nasrollahzadeh, M.; Atarod, M.; Sajjadi, M.; Sajadi, S.M.; Issaabadi, Z. *Plant-Mediated Green Synthesis of Nanostructures: Mechanisms, Characterization, and Applications*, 1st ed.; Elsevier: Amsterdam, The Netherlands, 2019; Volume 28.
24. Dash, A.; Ahmed, M.T.; Selvaraj, R. Mesoporous magnetite nanoparticles synthesis using the *Peltophorum pterocarpum* pod extract, their antibacterial efficacy against pathogens and ability to remove a pollutant dye. *J. Mol. Struct.* **2019**, *1178*, 268–273. [[CrossRef](#)]
25. Singh, J.; Dutta, T.; Kim, K.H.; Rawat, M.; Samddar, P.; Kumar, P. “Green” synthesis of metals and their oxide nanoparticles: Applications for environmental remediation. *J. Nanobiotechnol.* **2018**, *16*, 84. [[CrossRef](#)]
26. Potbhare, A.K.; Chaudhary, R.G.; Chouke, P.B.; Yerpude, S.; Mondal, A.; Sonkusare, V.N.; Rai, A.R.; Juneja, H.D. Phytosynthesis of nearly monodisperse CuO nanospheres using *Phyllanthus reticulatus*/*Conyza bonariensis* and its antioxidant/antibacterial assays. *Mater. Sci. Eng. C* **2019**, *99*, 783–793. [[CrossRef](#)] [[PubMed](#)]
27. Maheswari, K.C.; Reddy, P.S. Green Synthesis of Magnetite Nanoparticles through Leaf Extract of *Azadirachta indica*. *JACS Dir.* **2016**, *2*, 189–191.
28. Venkateswarlu, S.; Rao, Y.S.; Balaji, T.; Prathima, B.; Jyothi, N.V.V. Biogenic synthesis of Fe₃O₄ magnetic nanoparticles using plantain peel extract. *Mater. Lett.* **2013**, *100*, 241–244. [[CrossRef](#)]
29. Šuljagić, M.; Vulić, P.; Jeremić, D.; Pavlović, V.; Filipović, S.; Kilanski, L.; Lewinska, S.; Slawska-Waniewska, A.; Milenković, M.R.; Nikolić, A.S.; et al. The influence of the starch coating on the magnetic properties of nanosized cobalt ferrites obtained by different synthetic methods. *Mater. Res. Bull.* **2021**, *134*, 111117. [[CrossRef](#)]
30. Kumar, I.; Mondal, M.; Sakthivel, N. *Green Synthesis of Phytogenic Nanoparticles*; Elsevier: Amsterdam, The Netherlands, 2019; pp. 37–73.

31. Bano, S.; Nazir, S.; Nazir, A.; Munir, S.; Mahmood, T.; Afzal, M.; Ansari, F.L.; Mazhar, K. Microwave-assisted green synthesis of superparamagnetic nanoparticles using fruit peel extracts: Surface engineering, T_2 relaxometry, and photodynamic treatment potential. *Int. J. Nanomed.* **2016**, *11*, 3833–3848. [[CrossRef](#)]
32. Hezam, F.A.; Khalifa, N.O.; Nur, O.; Mustafa, M.A. Synthesis and magnetic properties of $Ni_{0.5}Mg_xZn_{0.5-x}Fe_2O_4$ ($0.0 \leq x \leq 0.5$) nanocrystalline spinel ferrites. *Mater. Chem. Phys.* **2021**, *257*, 123770. [[CrossRef](#)]
33. Dumani, D.S.; Cook, J.R.; Kubelick, K.P.; Luci, J.J.; Emelianov, S.Y. Photomagnetic Prussian blue nanocubes: Synthesis, characterization, and biomedical applications. *Nanomed. Nanotechnol. Biol. Med.* **2020**, *24*, 102138. [[CrossRef](#)]
34. Amiri, M.; Gholami, T.; Amiri, O.; Pardakhti, A.; Ahmadi, M.; Akbari, A.; Amanatfard, A.; Salavati-Niasari, M. The magnetic inorganic-organic nanocomposite based on $ZnFe_2O_4$ -Imatinib-liposome for biomedical applications, *in vivo* and *in vitro* study. *J. Alloys Compd.* **2020**, *849*, 156604. [[CrossRef](#)]
35. Escobar, A.M.; Pizzio, L.R.; Romanelli, G.P. Catalizadores Magnéticos Basados En Óxidos De Hierro: Síntesis, Propiedades Y Aplicaciones. *Cienc. Desarro.* **2018**, *10*, 79–101. [[CrossRef](#)]
36. Novoselova, L.Y. Nanoscale magnetite: New synthesis approach, structure and properties. *Appl. Surf. Sci.* **2021**, *539*, 148275. [[CrossRef](#)]
37. Shah Saqib, A.N.; Thu Huong, N.T.; Kim, S.W.; Jung, M.H.; Lee, Y.H. Structural and magnetic properties of highly Fe-doped ZnO nanoparticles synthesized by one-step solution plasma process. *J. Alloys Compd.* **2021**, *853*, 157153. [[CrossRef](#)]
38. Nikolova, M.P.; Chavali, M.S. Metal oxide nanoparticles as biomedical materials. *Biomimetics* **2020**, *5*, 27. [[CrossRef](#)]
39. Dhar, P.K.; Saha, P.; Hasan, M.K.; Amin, M.K.; Haque, M.R. Green synthesis of magnetite nanoparticles using *Lathyrus sativus* peel extract and evaluation of their catalytic activity. *Clean. Eng. Technol.* **2021**, *3*, 100117. [[CrossRef](#)]
40. Silvestri, C.; Silvestri, L.; Forcina, A.; Di Bona, G.; Falcone, D. Green chemistry contribution towards more equitable global sustainability and greater circular economy: A systematic literature review. *J. Clean. Prod.* **2021**, *294*, 126137. [[CrossRef](#)]
41. Wang, W.W.; Zhu, Y.J.; Ruan, M.L. Microwave-assisted synthesis and magnetic property of magnetite and hematite nanoparticles. *J. Nanoparticle Res.* **2007**, *9*, 419–426. [[CrossRef](#)]
42. Nüchter, M.; Müller, U.; Ondruschka, B.; Tied, A.; Lautenschläger, W. Microwave-assisted chemical reactions. *Chem. Eng. Technol.* **2003**, *26*, 1207–1216. [[CrossRef](#)]
43. Henam, S.D.; Ahmad, F.; Shah, M.A.; Parveen, S.; Wani, A.H. Microwave synthesis of nanoparticles and their antifungal activities. *Spectrochim. Acta Part A Mol. Biomol. Spectrosc.* **2019**, *213*, 337–341. [[CrossRef](#)]
44. Lazaratos, M.; Karathanou, K.; Mainas, E.; Chatzigoulas, A.; Pippa, N.; Demetzos, C.; Cournia, Z. Coating of magnetic nanoparticles affects their interactions with model cell membranes. *Biochim. Biophys. Acta Gen. Subj.* **2020**, *1864*, 129671. [[CrossRef](#)]
45. Hu, T.; Wang, Z.; Shen, W.; Liang, R.; Yan, D.; Wei, M. Recent advances in innovative strategies for enhanced cancer photodynamic therapy. *Theranostics* **2021**, *11*, 3278–3300. [[CrossRef](#)]
46. Estelrich, J.; Antònia Busquets, M. Iron oxide nanoparticles in photothermal therapy. *Molecules* **2018**, *23*, 1567. [[CrossRef](#)] [[PubMed](#)]
47. Hu, M.; Chen, J.; Li, Z.Y.; Au, L.; Hartland, G.V.; Li, X.; Marquez, M.; Xia, Y. Gold nanostructures: Engineering their plasmonic properties for biomedical applications. *Chem. Soc. Rev.* **2006**, *35*, 1084–1094. [[CrossRef](#)] [[PubMed](#)]
48. Patil, R.M.; Thorat, N.D.; Shete, P.B.; Bedge, P.A. Comprehensive cytotoxicity studies of superparamagnetic iron oxide nanoparticles. *Biochem. Biophys. Rep.* **2018**, *13*, 63–72. [[CrossRef](#)]
49. Peng, Y.; Xia, C.; Cui, M.; Yao, Z.; Yi, X. Effect of reaction condition on microstructure and properties of $(NiCuZn)Fe_2O_4$ nanoparticles synthesized via co-precipitation with ultrasonic irradiation. *Ultrason. Sonochem.* **2021**, *71*, 105369. [[CrossRef](#)]
50. Liu, Y.; Guo, Z.; Li, F.; Xiao, Y.; Zhang, Y.; Bu, T.; Jia, P.; Zhe, T.; Wang, L. Multifunctional Magnetic Copper Ferrite Nanoparticles as Fenton-like Reaction and Near-Infrared Photothermal Agents for Synergetic Antibacterial Therapy. *ACS Appl. Mater. Interfaces* **2019**, *11*, 31649–31660. [[CrossRef](#)] [[PubMed](#)]
51. Cordeiro, A.P.; Feuser, P.E.; Araújo, P.H.H.; Sayer, C. Encapsulation of Magnetic Nanoparticles and Copaíba Oil in Poly(methyl methacrylate) Nanoparticles via Miniemulsion Polymerization for Biomedical Application. *Macromol. Symp.* **2020**, *394*, 1–5. [[CrossRef](#)]
52. Hussain, S.M.; Hess, K.L.; Gearhart, J.M.; Geiss, K.T.; Schlager, J.J. *In vitro* toxicity of nanoparticles in BRL 3A rat liver cells. *Toxicol. Vitro.* **2005**, *19*, 975–983. [[CrossRef](#)]
53. Tousi, M.S.; Sepehri, H.; Khoee, S.; Farimani, M.M.; Delphi, L.; Mansourizadeh, F. Evaluation of apoptotic effects of mPEG-b-PLGA coated iron oxide nanoparticles as a eupatorin carrier on DU-145 and LNCaP human prostate cancer cell lines. *J. Pharm. Anal.* **2021**, *11*, 108–121. [[CrossRef](#)]
54. Alarifi, S.; Ali, D.; Alkahtani, S. Iron Oxide Nanoparticles Induce Oxidative Stress, DNA Damage, and Caspase Activation in the Human Breast Cancer Cell Line. *Biol. Trace Elem. Res.* **2014**, *159*, 416–424. [[CrossRef](#)]
55. Auffan, M.; Achouak, W.; Rose, J.; Roncato, M.-A.; Chanéac, C.; Waite, D.; Masion, A.; Woicik, J.; Wiesner, M.; Bottero, J.-Y. Relation between the Redox State of Iron-Based Nanoparticles and Their Cytotoxicity toward *Escherichia coli*. *Environ. Sci. Technol.* **2008**, *42*, 6730–6735. [[CrossRef](#)]
56. Wei, H.; Hu, Y.; Wang, J.; Gao, X.; Qian, X.; Tang, M. Superparamagnetic iron oxide nanoparticles: Cytotoxicity, metabolism, and cellular behavior in biomedicine applications. *Int. J. Nanomed.* **2021**, *16*, 6097–6113. [[CrossRef](#)]

57. Nel, A.E.; Mädler, L.; Velegol, D.; Xia, T.; Hoek, E.M.V.; Somasundaran, P.; Klaessig, F.; Castranova, V.; Thompson, M. Understanding biophysicochemical interactions at the nano-bio interface. *Nat. Mater.* **2009**, *8*, 543–557. [[CrossRef](#)]
58. Bobo, D.; Robinson, K.J.; Islam, J.; Thurecht, K.J.; Corrie, S.R. Nanoparticle-Based Medicines: A Review of FDA-Approved Materials and Clinical Trials to Date. *Pharm. Res.* **2016**, *33*, 2373–2387. [[CrossRef](#)]
59. Sharma, S.K. *Complex Magnetic Nanostructures: Synthesis, Assembly and Applications*; Springer: Berlin/Heidelberg, Germany, 2017.
60. Chen, B.W.; He, Y.C.; Sung, S.Y.; Le, T.T.H.; Hsieh, C.L.; Chen, J.Y.; Wei, Z.H.; Yao, D.J. Synthesis and characterization of magnetic nanoparticles coated with polystyrene sulfonic acid for biomedical applications. *Sci. Technol. Adv. Mater.* **2020**, *21*, 471–481. [[CrossRef](#)]
61. López-Téllez, G.; Balderas-Hernández, P.; Barrera-Díaz, C.E.; Vilchis-Nestor, A.R.; Roa-Morales, G.; Bilyeu, B. Green method to form iron oxide nanorods in orange peels for chromium (VI) reduction. *J. Nanosci. Nanotechnol.* **2013**, *13*, 2354–2361. [[CrossRef](#)] [[PubMed](#)]
62. Kahrilas, G.A.; Wally, L.M.; Fredrick, S.J.; Hiskey, M.; Prieto, A.L.; Owens, J.E. Microwave-Assisted Green Synthesis of Silver Nanoparticles Using Orange Peel Extract. *ACS Sustain. Chem. Eng.* **2013**, *2*, 367–376. [[CrossRef](#)]
63. Petcharoen, K.; Sirivat, A. Synthesis and characterization of magnetite nanoparticles via the chemical co-precipitation method. *Mater. Sci. Eng. B Solid-State Mater. Adv. Technol.* **2012**, *177*, 421–427. [[CrossRef](#)]
64. Saxena, N.; Singh, M. Efficient synthesis of superparamagnetic magnetite nanoparticles under air for biomedical applications. *J. Magn. Magn. Mater.* **2017**, *429*, 166–176. [[CrossRef](#)]
65. Rahmayanti, M. Synthesis of Magnetite Nanoparticles Using The Reverse Co-precipitation Method With NH_4OH as Precipitating Agent and Its Stability Test at Various pH. *Nat. Sci. J. Sci. Technol.* **2020**, *9*, 54–58. [[CrossRef](#)]
66. Wroblewski, C.; Volford, T.; Martos, B.; Samoluk, J.; Martos, P. High yield synthesis and application of magnetite nanoparticles (Fe_3O_4). *Magnetochemistry* **2020**, *6*, 22. [[CrossRef](#)]
67. Nnadozie, E.C.; Ajibade, P.A. Green synthesis and characterization of magnetite (Fe_3O_4) nanoparticles using *Chromolaena odorata* root extract for smart nanocomposite. *Mater. Lett.* **2020**, *263*, 127145. [[CrossRef](#)]
68. Raja, P.M.V.; Barron, A.R. Physical methods in chemistry. *Nature* **2019**, *134*, 366–367. [[CrossRef](#)]
69. Marrese, M.; Guarino, V.; Ambrosio, L. Atomic Force Microscopy: A Powerful Tool to Address Scaffold Design in Tissue Engineering. *J. Funct. Biomater.* **2017**, *8*, 7. [[CrossRef](#)] [[PubMed](#)]
70. Christensen, M.; Rasmussen, J.T.; Simonsen, A.C. Roughness analysis of single nanoparticles applied to atomic force microscopy images of hydrated casein micelles. *Food Hydrocoll.* **2015**, *45*, 168–174. [[CrossRef](#)]
71. Taimoory, S.M.; Rahdar, A.; Aliahmad, M.; Sadeghfard, F.; Hajinezhad, M.R.; Jahantigh, M.; Shahbazi, P.; Trant, J.F. The synthesis and characterization of a magnetite nanoparticle with potent antibacterial activity and low mammalian toxicity. *J. Mol. Liq.* **2018**, *265*, 96–104. [[CrossRef](#)]
72. Silva, V.A.J.; Andrade, P.L.; Silva, M.P.C.; Bustamante, A.D.; De Los Santos Valladares, L.; Albino Aguiar, J. Synthesis and characterization of Fe_3O_4 nanoparticles coated with fucan polysaccharides. *J. Magn. Magn. Mater.* **2013**, *343*, 138–143. [[CrossRef](#)]
73. Tomul, F.; Arslan, Y.; Başıoğlu, F.T.; Babuçcuoğlu, Y.; Tran, H.N. Efficient removal of anti-inflammatory from solution by Fe-containing activated carbon: Adsorption kinetics, isotherms, and thermodynamics. *J. Environ. Manag.* **2019**, *238*, 296–306. [[CrossRef](#)]
74. Akram, M.A.; Khan, B.A.; Khan, M.K.; Alqahtani, A.; Alshahrani, S.M.; Hosny, K.M. Fabrication and characterization of polymeric pharmaceutical emulgel co-loaded with eugenol and linalool for the treatment of trichophyton rubrum infections. *Polymers* **2021**, *13*, 3904. [[CrossRef](#)]
75. Schwaminger, S.P.; Syhr, C.; Berensmeier, S. Controlled synthesis of magnetic iron oxide nanoparticles: Magnetite or maghemite? *Crystals* **2020**, *10*, 214. [[CrossRef](#)]
76. Rečnik, A.; Nyir-Kósa, I.; Dódony, I.; Pósfai, M. Growth defects and epitaxy in Fe_3O_4 and $\gamma\text{-Fe}_2\text{O}_3$ nanocrystals. *CrystEngComm* **2013**, *15*, 7539–7547. [[CrossRef](#)]
77. Nemati, Z.; Khurshid, H.; Alonso, J.; Phan, M.H.; Mukherjee, P.; Srikanth, H. From core/shell to hollow $\text{Fe}/\gamma\text{-Fe}_2\text{O}_3$ nanoparticles: Evolution of the magnetic behavior. *Nanotechnology* **2015**, *26*, 405705. [[CrossRef](#)] [[PubMed](#)]
78. Phan, M.H.; Alonso, J.; Khurshid, H.; Lampen-Kelley, P.; Chandra, S.; Repa, K.S.; Nemati, Z.; Das, R.; Iglesias, Ó.; Srikanth, H. Exchange bias effects in iron oxide-based nanoparticle systems. *Nanomaterials* **2016**, *6*, 221. [[CrossRef](#)] [[PubMed](#)]
79. Slavov, L.; Abrashev, M.V.; Merodiiska, T.; Gelev, C.; Vandenberghe, R.E.; Markova-Deneva, I.; Nedkov, I. Raman spectroscopy investigation of magnetite nanoparticles in ferrofluids. *J. Magn. Magn. Mater.* **2010**, *322*, 1904–1911. [[CrossRef](#)]
80. Chamritski, I.; Burns, G. Infrared- And raman-active phonons of magnetite, maghemite, and hematite: A computer simulation and spectroscopic study. *J. Phys. Chem. B* **2005**, *109*, 4965–4968. [[CrossRef](#)] [[PubMed](#)]
81. Shebanova, O.N.; Lazor, P. Raman spectroscopic study of magnetite (FeFe_2O_4): A new assignment for the vibrational spectrum. *J. Solid State Chem.* **2003**, *174*, 424–430. [[CrossRef](#)]
82. Salviano, L.B.; Silva Cardoso, T.M.D.S.; Silva, G.C.; Silva Dantas, M.S.; Mello Ferreira, A.D.M. Microstructural assessment of magnetite nanoparticles (Fe_3O_4) obtained by chemical precipitation under different synthesis conditions. *Mater. Res.* **2018**, *21*. [[CrossRef](#)]
83. Jubb, A.M.; Allen, H.C. Vibrational spectroscopic characterization of hematite, maghemite, and magnetite thin films produced by vapor deposition. *ACS Appl. Mater. Interfaces* **2010**, *2*, 2804–2812. [[CrossRef](#)]

84. Yvon, H.J. Raman Spectroscopy for Analysis and Monitoring. Horiba Jobin Yvon, Raman Appl Note. 2017; pp. 1–2. Available online: <http://www.horiba.com/fileadmin/uploads/Scientific/Documents/Raman/bands.pdf> (accessed on 5 February 2022).
85. Mitchell, J. *Microscopic Identification of Organic Compounds*; Wiley: Hoboken, NJ, USA, 1949; Volume 21, pp. 448–461.
86. Rasouli, E.; Basirun, W.J.; Rezayi, M.; Shameli, K.; Nourmohammadi, E.; Khandanlou, R.; Izadiyan, Z.; Sarkarizi, H.K. Ultrasmall superparamagnetic Fe₃O₄ nanoparticles: Honey-based green and facile synthesis and *in vitro* viability assay. *Int. J. Nanomed.* **2018**, *13*, 6903–6911. [CrossRef]
87. Nurbas, M.; Ghorbanpoor, H.; Avci, H. An eco-friendly approach to synthesis and characterization of magnetite (Fe₃O₄) nanoparticles using *Platanus Orientalis* L. leaf extract. *Dig. J. Nanomater. Biostruct.* **2017**, *12*, 993–1000.
88. Lobato, N.C.C.; Mansur, M.B.; De Mello Ferreira, A. Characterization and chemical stability of hydrophilic and hydrophobic magnetic nanoparticles. *Mater. Res.* **2017**, *20*, 736–746. [CrossRef]
89. Guardia, P.; Batlle-Brugal, B.; Roca, A.G.; Iglesias, O.; Morales, M.P.; Serna, C.J.; Labarta, A.; Batlle, X. Surfactant effects in magnetite nanoparticles of controlled size. *J. Magn. Magn. Mater.* **2007**, *316*, 756–759. [CrossRef]
90. Kemp, S.J.; Ferguson, R.M.; Khandhar, A.P.; Krishnan, K.M. Monodisperse magnetite nanoparticles with nearly ideal saturation magnetization. *RSC Adv.* **2016**, *6*, 77452–77464. [CrossRef]
91. Wei, Y.; Han, B.; Hu, X.; Lin, Y.; Wang, X.; Deng, X. Synthesis of Fe₃O₄ nanoparticles and their magnetic properties. *Procedia Eng.* **2012**, *27*, 632–637. [CrossRef]
92. Millan, A.; Urtizberea, A.; Silva, N.J.O.; Palacio, F.; Amaral, V.S.; Snoeck, E.; Serin, V. Surface effects in maghemite nanoparticles. *J. Magn. Magn. Mater.* **2007**, *312*, L5–L9. [CrossRef]
93. Sánchez, O.; Universidad Nacional Mayor de San Marcos. Medicina (B Aires). Available online: http://cybertesis.unmsm.edu.pe/bitstream/handle/cybertesis/4147/Diaz_rc.pdf;jsessionid=CD5A7FF3022F1A5526948369A600356D?sequence=1 (accessed on 12 September 2022).
94. Bedanta, S.; Petravic, O.; Kleemann, W. *Supermagnetism*; Elsevier: Amsterdam, The Netherlands, 2015; Volume 23.
95. Livesey, K.L.; Ruta, S.; Anderson, N.R.; Baldomir, D.; Chantrell, R.W.; Serantes, D. Beyond the blocking model to fit nanoparticle ZFC/FC magnetisation curves. *Sci. Rep.* **2018**, *8*, 11166. [CrossRef] [PubMed]
96. Guldris, N.; Argibay, B.; Gallo, J.; Iglesias-Rey, R.; Carbó-Argibay, E.; Kolen'Ko, Y.V.; Campos, F.; Sobrino, T.; Salonen, L.M.; Bañobre-López, M.; et al. Magnetite Nanoparticles for Stem Cell Labeling with High Efficiency and Long-Term *in vivo* Tracking. *Bioconjug. Chem.* **2017**, *28*, 362–370. [CrossRef] [PubMed]
97. Padmanabhan, S.K.; Nitti, P.; Stanca, E.; Rochira, A.; Siculella, L.; Raucci, M.G.; Madaghiele, M.; Licciulli, A.; Demitri, C. Mechanical and biological properties of magnesium-and silicon-substituted hydroxyapatite scaffolds. *Materials* **2021**, *14*, 6942. [CrossRef]
98. Li, Y.; Wang, Z.; Liu, R. Superparamagnetic α -Fe₂O₃/Fe₃O₄ heterogeneous nanoparticles with enhanced biocompatibility. *Nanomaterials* **2021**, *11*, 834. [CrossRef]
99. Hedayatnasab, Z.; Dabbagh, A.; Abnisa, F.; Wan Daud, W.M.A. Synthesis and *in-vitro* characterization of superparamagnetic iron oxide nanoparticles using a sole precursor for hyperthermia therapy. *Mater. Res. Bull.* **2020**, *132*, 110975. [CrossRef]
100. Bhardwaj, A.; Jain, N.; Parekh, K. Investigating the effect of outer layer of magnetic particles on cervical cancer cells HeLa by magnetic fluid hyperthermia. *Cancer Nanotechnol.* **2021**, *12*, 7. [CrossRef]
101. Huang, J.; Luo, C.; Li, W.; Li, Y.; Zhang, Y.S.; Zhou, J.; Jiang, Q. Eccentric magnetic microcapsules for orientation-specific and dual stimuli-responsive drug release. *J. Mater. Chem. B* **2015**, *3*, 4530–4538. [CrossRef] [PubMed]
102. Jangamreddy, J.R.; Los, M.J. Mitoptosis, a novel mitochondrial death mechanism leading predominantly to activation of autophagy. *Hepat. Mon.* **2012**, *12*, 10–12. [CrossRef]
103. Yusefi, M.; Shameli, K.; Yee, O.S.; Teow, S.Y.; Hedayatnasab, Z.; Jahangirian, H.; Webster, T.J.; Kuča, K. Green synthesis of Fe₃O₄ nanoparticles stabilized by a *Garcinia mangostana* fruit peel extract for hyperthermia and anticancer activities. *Int. J. Nanomed.* **2021**, *16*, 2515–2532. [CrossRef] [PubMed]
104. Noval, V.E.; Puentes, C.O.; Carriazo, J.G. Magnetita (Fe₃O₄): Uma estrutura inorgânica com múltiplas aplicações em catálise heterogênea. *Rev. Colomb. Quim.* **2017**, *46*, 42–59.
105. Frey, P.A.; Reed, G.H. The ubiquity of iron. *ACS Chem. Biol.* **2012**, *7*, 1477–1481. [CrossRef] [PubMed]
106. Martinelli, C.; Pucci, C.; Ciofani, G. Nanostructured carriers as innovative tools for cancer diagnosis and therapy. *APL Bioeng.* **2019**, *3*, 011502. [CrossRef] [PubMed]
107. Wiart, M.; Tavakoli, C.; Hubert, V.; Hristovska, I.; Dumot, C.; Parola, S.; Lerouge, F.; Chauveau, F.; Canet-Soulas, E.; Pascual, O.; et al. Use of metal-based contrast agents for *in vivo* MR and CT imaging of phagocytic cells in neurological pathologies. *J. Neurosci. Methods* **2023**, *383*, 109729. [CrossRef]
108. Romero, M.P.; Marangoni, V.S.; de Faria, C.G.; Leite, I.S.; Silva, C.D.C.C.E.; Maroneze, C.M.; Pereira-da-Silva, M.A.; Bagnato, V.S.; Inada, N.M. Graphene Oxide Mediated Broad-Spectrum Antibacterial Based on Bimodal Action of Photodynamic and Photothermal Effects. *Front. Microbiol.* **2020**, *10*, 2995. [CrossRef]
109. Ashkbar, A.; Rezaei, F.; Attari, F.; Ashkevarian, S. Treatment of breast cancer *in vivo* by dual photodynamic and photothermal approaches with the aid of curcumin photosensitizer and magnetic nanoparticles. *Sci. Rep.* **2020**, *10*, 21206. [CrossRef]
110. Sundaram, P.; Abrahamse, H. Phototherapy combined with carbon nanomaterials (1D and 2D) and their applications in cancer therapy. *Materials* **2020**, *13*, 4830. [CrossRef]

111. Qing, G.; Zhao, X.; Gong, N.; Chen, J.; Li, X.; Gan, Y.; Wang, Y.; Zhang, Z.; Zhang, Y.; Guo, W.; et al. Thermo-responsive triple-function nanotransporter for efficient chemo-photothermal therapy of multidrug-resistant bacterial infection. *Nat. Commun.* **2019**, *10*, 4336. [[CrossRef](#)] [[PubMed](#)]
112. Mascolo, M.C.; Pei, Y.; Ring, T.A. Room Temperature Co-Precipitation Synthesis of Magnetite Nanoparticles in a Large pH Window with Different Bases. *Materials* **2013**, *6*, 5549–5567. [[CrossRef](#)] [[PubMed](#)]
113. Hussein-Al-Ali, S.H.; El Zowalaty, M.E.; Hussein, M.Z.; Geilich, B.M.; Webster, T.J. Synthesis, characterization, and antimicrobial activity of an ampicillin-conjugated magnetic nanoantibiotic for medical applications. *Int. J. Nanomed.* **2014**, *9*, 3801–3814. [[CrossRef](#)]
114. Luz, M.; Piscioti, M. Estudio del proceso de calentamiento de nanopartículas magnéticas con campos magnéticos AC para su utilización en el tratamiento de tumores por hipertermia. Ph.D. Thesis, Universidad Nacional de Cuyo, Mendoza, Argentina, 2009.
115. Zheng, B.; Zhang, M.; Xiao, D.; Jin, Y.; Choi, M.M.F. Fast microwave synthesis of Fe₃O₄ and Fe₃O₄/Ag magnetic nanoparticles using Fe²⁺ as precursor. *Inorg. Mater.* **2010**, *46*, 1106–1111. [[CrossRef](#)]
116. Alamar, B. *Resazurin Cell Viability Assay Kit*; Biotium Glowing Products for Science: Fremont, CA, USA, 2015; Volume 14998, pp. 1919–1920.
117. Bioarray, C. Resazurin Cell Viability Assay. 2022. Available online: <https://www.creative-bioarray.com/support/resazurin-cell-viability-assay.htm> (accessed on 12 September 2022).

Disclaimer/Publisher’s Note: The statements, opinions and data contained in all publications are solely those of the individual author(s) and contributor(s) and not of MDPI and/or the editor(s). MDPI and/or the editor(s) disclaim responsibility for any injury to people or property resulting from any ideas, methods, instructions or products referred to in the content.